Chinese Chemical Letters 37 (2026) 112456

Contents lists available at ScienceDirect

Chinese Chemical Letters

journal homepage: www.elsevier.com/locate/cclet

Surface and interfacial engineering in photocatalytic water splitting: Catalyst design strategies and mechanisms

Xue Zhang [a,1], Zixuan Zhang [b,1], Zongyang Ya [b,1], Shengbo Zhang [c,*], Hua Wang [b,*]

[a] College of Medical Imaging, Qilu Medical University, Zibo 255300, China
[b] Key Laboratory for Green Chemical Technology of Ministry of Education, Collaborative Innovation Center of Chemical Science and Engineering, School of Chemical Engineering and Technology, Tianjin University, Tianjin 300072, China
[c] School of Environmental Science and Engineering, Tianjin Key Laboratory of Biomass/Wastes Utilization, Tianjin University, Tianjin 300350, China

ARTICLE INFO

Article history:
Received 16 December 2025
Revised 19 January 2026
Accepted 23 January 2026
Available online 23 January 2026

Keywords:
Photocatalytic water splitting
Surface and interfacial engineering
Heteroatom doping
Functional group modification
Heterostructure construction

ABSTRACT

Photocatalytic water splitting provides a sustainable approach for converting solar energy into H_2. Surface and interfacial engineering has become crucial strategies for enhancing photochemical efficiency and optimizing active sites. This review outlines several primary design strategies, including heteroatom doping (encompassing nonmetal and metal atomic doping), functional group modification, defect engineering, and heterostructure construction. These strategies aim to improve charge separation and surface reaction efficiency. The mechanistic roles of these strategies in metal oxides, sulfides, and carbon nitrides are discussed in terms of band structure tuning, the formation of electron transport pathways, and the modulation of intermediate adsorption energetics. The review examines the synergistic effects of these strategies in enhancing photocatalytic efficiency, stability, and environmental adaptability. Finally, we address future challenges, including interfacial structural stability, *in situ* characterization of reaction dynamics, and potential applications in sustainable energy systems. We believe that this review will provide insights into developing high-performance photocatalysts for water splitting.

© 2026 Published by Elsevier B.V. on behalf of Chinese Chemical Society and Institute of Materia Medica, Chinese Academy of Medical Sciences.

1. Introduction

With the continuous growth in global energy demand, the depletion of fossil fuel resources, and worsening environmental pollution, these challenges have become increasingly pressing [1,2]. Hydrogen (H_2) has been identified as a promising sustainable energy source, with considerable attention drawn to it due to its high efficiency and environmental friendliness [3–6]. During combustion, H_2 produces only water, with no concomitant emissions of pollutants or greenhouse gases. Current primary methods for H_2 evolution include fossil fuel reforming [7–9], industrial by-product H_2 recovery [10–12], biomass-based H_2 evolution [13–16], and water electrolysis [17–21]. Compared with conventional approaches, photocatalytic water splitting offers a sustainable alternative that uses only solar energy and water as feedstock [22]. This process directly converts solar energy into chemical energy by splitting water into H_2 and oxygen (O_2) without consuming fossil fuels, thereby avoiding carbon emissions and other pollutants. Consequently, it provides a clean, stable, and sustainable method for H_2 evolution [23–27].

Despite significant progress, the field of photocatalytic water splitting continues to grapple with challenges that impede its widespread adoption, such as enhancing efficiency, reducing costs, and ensuring long-term stability. The core issues lie in the photocatalyst system itself. Conventional photocatalysts generally suffer from a limited light absorption range, severe charge carrier recombination, and sluggish surface reaction kinetics [28–30]. During photocatalysis, when the photocatalyst is irradiated with light, photogenerated electron-hole pairs are formed. However, these charge carriers tend to recombine before participating in chemical reactions, thereby reducing the number of active carriers available for the reactions. Consequently, this decreases photocatalytic efficiency and leads to the loss of solar energy [31]. Furthermore, conventional photocatalytic systems often lack sufficient active sites. These active sites are crucial for the water splitting reaction. Their insufficient quantity directly limits the efficiency of surface redox reactions, severely hindering overall photocatalytic performance [32]. Additionally, photocatalysts may experience structural and performance degradation due to photo-corrosion or chemical corrosion during photocatalytic reactions, which reduces their service lifetime and stability. This not only increases costs but also restricts

* Corresponding authors.
E-mail addresses: shengbozhang@tju.edu.cn (S. Zhang), tjuwanghua@tju.edu.cn (H. Wang).
[1] These authors contributed equally to this work.

https://doi.org/10.1016/j.cclet.2026.112456
1001-8417/© 2026 Published by Elsevier B.V. on behalf of Chinese Chemical Society and Institute of Materia Medica, Chinese Academy of Medical Sciences.

the practical application of photocatalytic water splitting technology [33–35]. Scalable photocatalytic water splitting has gained significant attention, highlighted by the successful demonstration of a 100 m^2 panel reactor array. This system maintained stable and safe operation under field conditions for several months. Although the solar-to-hydrogen (STH) efficiency remained below 1 %, the work confirmed the practical feasibility of large-area H_2 evolution, gas collection, and separation [36]. However, the study identified poor charge separation, sluggish interfacial kinetics, and insufficient stability as primary bottlenecks. These findings highlight that surface and interfacial processes are central to the efficiency and stability of large-scale photocatalytic systems. Therefore, overcoming these challenges within photocatalyst systems is pivotal for advancing photocatalytic H_2 evolution towards large-scale industrialization.

Surface and interfacial engineering emerges as a key design strategy for enhancing photocatalytic performance [37]. The surface of a photocatalyst is the part that directly interacts with the external environment, influencing the behavior of photogenerated charge carriers. For instance, surface defect structures can affect the separation and migration rates of charge carriers. The interface is the transition region between different materials. When a photocatalyst is composed of multiple materials, the interfaces significantly influence charge transfer and photocatalytic reactions. In heterostructured photocatalysts, the interface between different materials induces band bending. This generates a built-in electric field, which facilitates the separation of photogenerated electron-hole pairs and reduces the probability of charge carrier recombination. Surface and interfacial engineering has been shown to optimize the physicochemical properties of the surface and interfaces, including the electronic structure, surface chemistry and the environment of active sites. Therefore, they can enhance light absorption efficiency, facilitate charge migration, and optimize reaction pathways, ultimately improving photocatalytic performance efficiency [38–40]. Scientists have developed various strategies for the surface and interfacial engineering of photocatalysts. For instance, heteroatom doping facilitates the refinement of the band structure and modulates the charge state of the catalyst [41]. Functional group modification enables the adjustment of the adsorption energy of intermediates and improves reaction selectivity [42]. Defect engineering introduces active sites and local electric fields while maintaining crystal stability [43]. Metal nanoparticle loading facilitates electron extraction by forming Schottky junctions [44]. Furthermore, heterostructure construction leverages band alignment and built-in electric fields to achieve efficient charge separation [45]. These strategies significantly enhance both the activity and stability of photocatalytic water splitting systems.

Several recent reviews have addressed the challenges of photocatalytic H_2 evolution from diverse perspectives. For instance, specific works have provided broad overviews of preparation strategies and the potential for seawater splitting [46,47]. Others have focused on specialized reaction systems including gas-solid biphase systems for water vapor splitting [48]. Research has also examined the coupling of H_2 evolution with value-added oxidation reactions [49]. Furthermore, historical developments in overall water splitting (OWS) efficiency [50] and the optimization of photoelectrocatalytic (PEC) systems [51] have been systematically documented. These reviews offer valuable insights into specific reaction types and system architectures. However, a dedicated and comprehensive discussion centered on the synergistic relationship between surface and interfacial engineering remains critical. Unlike previous works that prioritize general material preparation or reactor design, this review focuses specifically on surface and interfacial modulation strategies.

In this review, we summarize the latest advances in surface and interfacial engineering of photocatalysts for photocatalytic water splitting to produce H_2 (Fig. 1). We discuss in detail several key design strategies, including heteroatom doping (both nonmetal and metal dopants), functional group modification, defect engineering, and heterostructure construction. The mechanistic roles of these strategies in photocatalytic materials are thoroughly analyzed. The discussion emphasizes on band structure regulation, electron transport pathways, and intermediate adsorption energetics. Furthermore, we explore the potential synergistic effects among these strategies and discuss the current challenges and future directions in photocatalytic H_2 evolution. We expect this review will provide valuable insights and guidance for the design and development of novel photocatalytic water splitting systems, thereby advancing research on photocatalytic H_2 evolution.

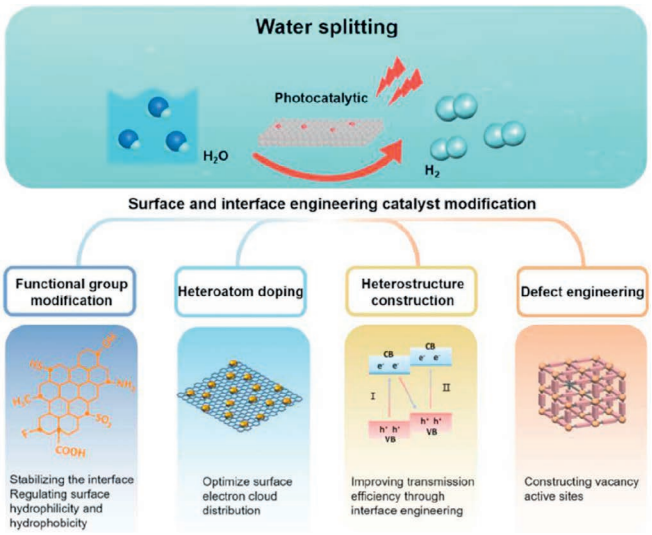


Fig. 1. Surface and interface engineering modifies photocatalysts through various strategies to promote water splitting and achieve efficient H_2 evolution.

2. Surface and interfacial engineering for photocatalytic systems

2.1. Photocatalyst materials and reactor platforms

Photocatalysts for water splitting span a broad range of material platforms, including metal oxides, metal sulfides, polymeric carbon nitride (g-C_3N_4), metal-organic frameworks (MOFs), covalent organic frameworks (COFs), and two-dimensional MXene materials. Despite their diverse compositions and crystal structures, the photocatalytic performance of these materials is ultimately governed by surface and interfacial processes, where light-driven charge carriers are separated, transported, and consumed by interfacial redox reactions. Consequently, surface and interfacial engineering has emerged as a strategy to overcome intrinsic material limitations and enable efficient and durable photocatalytic H_2 evolution.

Metal oxide photocatalysts represent the most classical and widely studied systems in photocatalytic water splitting [52–54]. Their band edge positions are generally well matched to the redox potentials of water, and their robust crystal lattices provide exceptional chemical and photochemical stability. However, the wide bandgaps and rapid bulk and surface charge recombination of most metal oxides severely limit their utilization of solar energy.

Metal sulfide photocatalysts, characterized by narrower bandgaps and strong visible-light absorption, inherently offer improved photon utilization compared with metal oxides [55–57]. Nevertheless, their practical deployment is constrained by severe photocorrosion, which originates from unfavorable interfacial oxidation processes driven by photogenerated holes.

Table 1
Comparison of surface and interfacial engineering strategies for photocatalytic water splitting.

Modification Strategy	Optimization mechanisms	Advantages	Limitations
Heteroatom doping	Band structure tuning, charge state modulation, formation of localized electronic states	Versatile, low cost (nonmetal/transition metal), synergistic with other strategies	Valence state instability (transition metal), low substitution efficiency (nonmetal), high cost (noble metal)
Functional group modification	Regulating electronic structure, optimizing interface hydrophilicity, constructing active sites	High targeting precision, low modification cost, structural tunability	Poor long-term stability (*e.g.*, -OH instability), limited independent contribution
Defect engineering	Introducing active sites, forming local electric fields, extending light absorption range	Enhances charge separation, modulates surface reaction kinetics	Precise control difficulty, deep-level defects as recombination centers, structural collapse risk
Heterostructure construction	Band alignment matching, built-in electric-field regulation, directional charge transfer	Preserves redox capability (S/Z-scheme), high active site density	Complex synthesis, interfacial recombination losses, lattice mismatch issues

The g-C_3N_4 exemplifies a material system in which interfacial regulation is critical to unlocking intrinsic potential [58–61]. Although g-C_3N_4 possesses a suitable bandgap for visible-light-driven H_2 evolution, its bulk charge recombination and limited surface active sites restrict performance. Surface functionalization, defect engineering, and heterojunction formation have been widely adopted to modulate surface electronic states, enhance charge separation, and optimize proton reduction kinetics. Importantly, g-C_3N_4 readily forms intimate interfaces with metals, metal oxides, and other semiconductors, allowing interfacial electric fields and band alignment effects to be exploited for directional charge transport.

For MOFs and COFs, the catalytic behavior is even more strongly dictated by surface and interfacial characteristics [62,63]. Their high porosity and structural tunability provide abundant interfacial sites for mass transport and catalytic reactions, while their modular architectures enable precise control over interfacial electronic coupling through ligand and node engineering. However, the stability and charge transport efficiency of these materials are often limited by interfacial hydrolysis, weak electronic connectivity, or inefficient carrier extraction. Surface modification, composite formation, and interfacial coupling with conductive or semiconducting phases are therefore indispensable for translating their structural advantages into practical photocatalytic activity.

Two-dimensional MXenes further highlight the central importance of interfacial engineering in photocatalysis [64,65]. Owing to their metallic conductivity and rich surface terminations, MXenes rarely function as standalone photocatalysts but serve as highly effective interfacial components. When integrated with semiconductor photocatalysts, MXenes can form Schottky or Z-scheme interfaces that facilitate ultrafast electron extraction, suppress recombination, and tune surface redox activity through work function modulation. Their role is inherently interfacial, acting as charge mediators and catalytic platforms rather than primary light absorbers.

While significant progress has been made in photocatalyst design, the efficiency and scalability of photocatalytic systems remain constrained by device engineering and system integration. Recent innovations in photothermal-photocatalytic devices and large-scale demonstrations have established a critical foundation for this technology [24]. At the laboratory level, core equipment includes quartz batch reactors equipped with solar simulators for standardized activity assessment, as well as fixed-bed reactors utilizing immobilized thin-film photocatalysts to prevent slurry sedimentation and simplify catalyst recovery. Industrial-scale demonstrations have achieved remarkable scaling. For gas separation, commercial polyimide hollow-fiber membranes have been implemented. Advanced industrial setups also incorporate parabolic trough concentrators to enhance light intensity, integrated with thermal management systems to prevent catalyst deactivation under high temperatures. Core auxiliary equipment further includes solar tracking systems, gas-liquid separation modules, modular photocatalyst sheet manufacturing equipment, and *in situ* monitoring devices [66]. Despite these advancements, the development of low-cost, durable, and efficient equipment remains a bottleneck, particularly the demand for scalable reactor materials. Addressing these device-related challenges is essential for advancing photocatalytic water splitting from laboratory demonstrations to industrial-scale applications.

2.2. The fundamentals of surface and interfacial engineering in photocatalytic water splitting

Surface and interfacial engineering involves modulating the atomic structure, chemical composition, charge distribution, and energy band alignment at the surface and interfacial regions. These modifications enhance the physicochemical properties of the materials [37–39]. In photocatalytic water splitting systems, the catalyst surface serves as the direct reaction site, influencing reactant adsorption, activation, and light absorption [51]. The interface plays a crucial role in the separation and migration of photogenerated electrons and holes. Surface engineering refers to the modification and reconstruction of a catalyst's surface using various strategies, including heteroatom doping (encompassing nonmetal and metal atomic doping), functional group modification, defect engineering, and heterostructure construction (Table 1). Interfacial engineering focuses on systems composed of two or more distinct phases, such as semiconductor-metal, semiconductor-semiconductor, or semiconductor-electrolyte interfaces. Enhanced charge carrier separation and interfacial stability is achieved by modulating interfacial coupling and charge transfer efficiency. The performance of photocatalysts is primarily determined by their surface and interfacial properties. Surface and interfacial engineering is not a set of independent processes. Surface modification affects interfacial band alignment, while interfacial optimization regulates the chemical environment of surface active sites.

In photocatalytic water splitting systems, the primary functions of surface and interfacial engineering are manifested in three aspects. These include modulation of band structures, facilitation of charge carrier separation and migration, and optimization of surface reaction kinetics (Fig. 2).

(1) Modulation of band structures: The band structure of a photocatalyst, including the energy positions of the conduction band (CB) and valence band (VB), directly affects its redox capability. The bandgap width determines the range of absorbable light wavelengths, while the density of states influences the absorption efficiency [67]. A photocatalyst can only utilize photons with energy greater than its bandgap to excite electrons from the VB to the CB, thereby generating

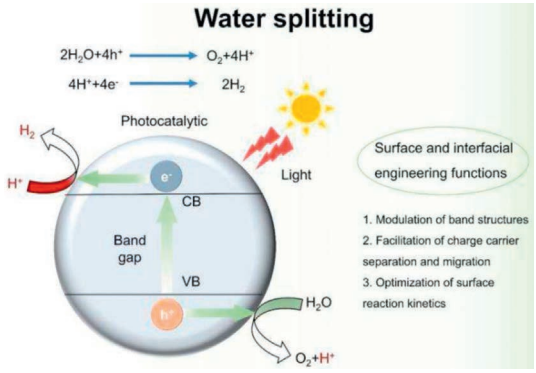


Fig. 2. Solar H_2 evolution from water using photocatalysts, and the role of surface and interface engineering in optimizing water splitting reactions.

photogenerated electron-hole pairs [68–70]. Wide-bandgap materials, such as TiO_2, absorb only ultraviolet light, resulting in low solar energy efficiency. Narrow-bandgap materials absorb visible light [71]. However, their redox ability weakens due to elevated CB and lowered VB potentials. Thus, a narrower bandgap is not necessarily better. In the photocatalytic water splitting reactions, the hydrogen evolution reaction (HER) and the oxygen evolution reaction (OER), the CB minimum must be more negative than the reduction potential of H^+/H_2, so that photogenerated electrons reduce protons to H_2. Meanwhile, the VB maximum must be more positive than the oxidation potential of O_2/H_2O to enable photogenerated holes to oxidize water to O_2.

(2) Charge carrier separation and migration: The behavior of photogenerated electron-hole pairs is closely related to photocatalytic efficiency [28]. After their generation, the recombination of these pairs leads to energy loss This process renders them unable to participate in reactions. In pure semiconductor materials, typically <10% of the photogenerated charge carriers contribute to the reactions. Furthermore, the recombination process accelerates surface structural degradation of the catalyst, thereby reducing its stability. Charge carrier migration involves two processes: bulk migration from the interior to the surface and interfacial migration across different material interfaces [70]. The migration efficiency depends on the migration rate and migration distance. The crystal structure and dimensions of the photocatalyst influence the charge carrier migration rate and recombination probability during bulk migration [67]. Therefore, promoting the efficient separation and migration of photogenerated charge carriers through surface and interfacial engineering can significantly enhance photocatalytic efficiency.

(3) Optimization of surface reaction kinetics: The catalyst surface serves as a platform for water molecule adsorption, dissociation, and H_2/O_2 evolution. The number and type of active sites on the catalyst surface directly influence the reaction rate [72]. The surface area is closely related to the number of active sites, and surface defects can generate additional active sites. Surface functional groups, defects, and cocatalysts can modulate the adsorption energy of reaction intermediates [73], thereby lowering reaction barriers. Thus, surface and interfacial engineering enhances photocatalytic efficiency at the macroscopic level. It determines the relationship between electronic structure, reaction activity, and stability at the microscopic level. To achieve efficient photocatalytic water splitting, researchers have proposed various surface and interfacial engineering strategies.

3. Heteroatom doping

Heteroatom doping involves introducing metal (*e.g.*, Fe, Co, Ni, Mo) or non-metal (*e.g.*, N, C, S, P) atoms into the catalyst lattice or onto its surface. This process effectively modulates the material's photocatalytic properties and surface reaction kinetics, making it one of the key strategies for improving the performance of photocatalytic water splitting.

3.1. Metal doping

Noble metals exhibit excellent electrical conductivity and catalytic activity. Doping noble metals into photocatalytic systems can create efficient charge-separation pathways and enhance surface reaction activity. Among them, platinum (Pt) is one of the most representative noble-metal dopants. Pt doping enhances photocatalytic performance by narrowing the catalyst bandgap, increasing electron storage capacity, and suppressing electron-hole recombination. De Lasa *et al.* synthesized Pt-doped TiO_2, finding that 2.50 wt% Pt loading yielded the highest H_2 evolution with a 22.6% quantum yield [53]. The Pt dopants reduced the bandgap and increased electron storage, which significantly inhibited electron-hole recombination. Li *et al.* doped Pt into Cs_2SnBr_6 perovskite, creating $Cs_2Pt_{0.25}Sn_{0.75}Br_6$ (Fig. 3A) [74]. This material achieved an H_2 evolution rate of 11.49 mmol g^{-1} h^{-1} in water without hydrohalic acid. Pt doping modulated surface active sites and enhanced stability in water of photocatalytic. The mechanism of noble metal doping is primarily associated with their high work function and surface plasmon resonance effects. These properties enable noble metals to act as effective electron trapping centers, promoting the separation and transfer of photogenerated charges. Although noble-metal doping exhibits excellent performance, its high cost and scarcity limit large-scale applications.

Transition metals (Fe, Ni, Mn, Cu, Mo, Cr, *etc.*) possess partially filled d orbitals, which allow them to form localized electronic states within the catalyst lattice, facilitating band structure modulation, directional charge-carrier separation, and optimization of surface reaction pathways. With significantly lower costs than noble metals, they demonstrate broader application prospects.

Esposito *et al.* prepared Fe-doped CeO_2, where doping narrowed the bandgap and increased oxygen vacancies, prolonging the carrier lifetime and achieving an H_2 evolution of 7566 μmol/L in 240 min [54]. Jin *et al.* constructed a heterojunction with Ni-doped CdS, where Ni shifted the d-band center and enhanced H^+ adsorption [55]. The H_2 evolution rate reached 13.33 mmol h^{-1} g^{-1}, 2.21 times higher than the undoped sample. The doping and loading of Ni synergistically optimized charge separation and surface reaction kinetics. He *et al.* doped Mn^{2+} into $ZnIn_2S_4$ and used a magnetic field to create spatially separated charge regions for oxidation and the HER, achieving an H_2 evolution rate 13.87 times higher than pure ZIS [75]. Dou *et al.* combined Mo doping with sulfur vacancies in $ZnIn_2S_4$, creating electron-rich and hole-rich regions for spatial separation of HER and oxidation [76,77]. Mo doping enhanced the H_2 evolution rate by 18.6 times and accelerated oxidation by 34.9 times. Zeng *et al.* prepared Cr-doped ZnS, where Cr^{3+} enriched holes and sulfur vacancies trapped electrons, synergistically optimizing reaction barriers and achieving HER activity 2.9 times higher than pure ZnS (Fig. 3B) [78].

Transition-metal doping offers a low-cost, versatile strategy for tuning photocatalyst properties. It can synergistically enhance performance when combined with defect engineering or heterostructure construction. However, it also presents notable limitations. Transition metals readily form multiple valence states (*e.g.*, Mn^{2+}/Mn^{4+}, Mo^{4+}/Mo^{6+}), which may exert opposite effects. Achieving uniformly distributed dopants is difficult, and designs that rely on gradients or localized enrichment lack broad applica-

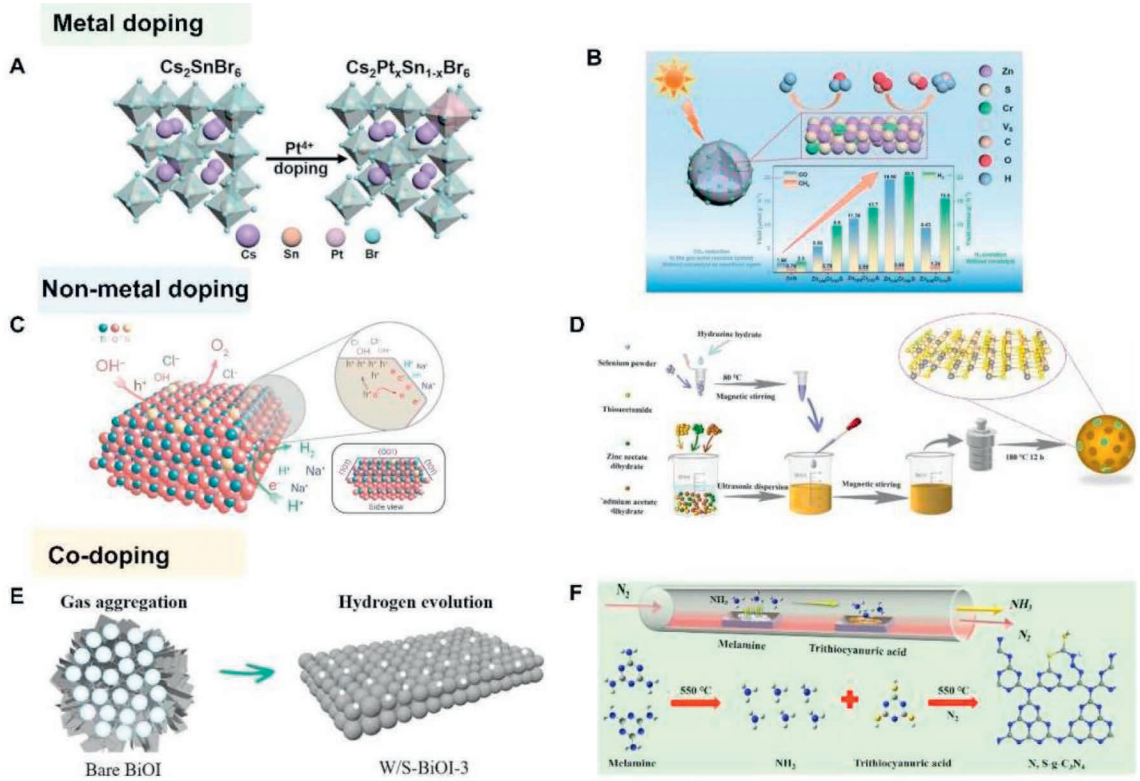


Fig. 3. Representative schematic illustrations of metal doping, non-metal doping, and co-doping. (A) Schematic illustration of the Pt-doped Cs_2SnBr_6 crystal structure as a representative noble-metal doping system. Reprinted with permission [74]. Copyright 2024, American Chemical Society. (B) Schematic illustration of Cr-dopant-induced photohole concentration and its enhancement of H_2 evolution efficiency. Reprinted with permission [78]. Copyright 2024, Elsevier. Representative surface polarization illustration: (C) Schematic illustration of electrolyte-assisted charge polarization on facet-controlled N-TiO_2 in seawater under photoexcitation. Reprinted with permission [81]. Copyright 2024, Springer Nature. (D) Schematic illustration of the synthesis route for Se-doped ZnCdS. Reprinted with permission [86]. Copyright 2024, Elsevier. Representative co-doping examples: (E) Schematic illustration of the difference in bubble evolution behavior before and after W/S co-doping. Reprinted with permission [89]. Copyright 2024, Elsevier. (F) Schematic illustration of the preparation of N, S-co-doped g-C_3N_4. Reprinted with permission [90]. Copyright 2025, Elsevier.

bility. Transition-metal ions are also prone to oxidation and migration under photogenerated holes, leading to the loss of active sites and raises concerns about long-term stability. Overall, transition-metal doping is advantageous for its low cost and strong tunability. It is well-suited for constructing synergistic systems. Nevertheless, practical applications require addressing key challenges, including valence-state instability, limited controllability, and insufficient long-term durability.

Rare-earth metals and other metals (*e.g.*, Sc, Ga) optimize photocatalysts through defect passivation or heterostructure construction. Liu *et al.* prepared Sc-doped TiO_2, where Sc^{3+} passivated harmful defects and the facet junction generated a strong built-in electric field, enabling spontaneous exciton dissociation [79]. Rare-earth-doped materials are relatively expensive and prone to phase separation, making them more suitable for advanced heterostructure design.

3.2. Non-metal doping

Non-metal doping is a core strategy for optimizing photocatalytic performance. It leverages advantages such as high atomic radius compatibility, precise electronic structure modulation, and low cost. Different non-metal elements (N, P, S, B, C, O, *etc.*) enhance band structure regulation, charge separation, and surface reaction kinetics. These improvements occur by substituting atoms in the catalyst lattice, introducing defects, or forming new chemical bonds.

N doping enhances photocatalytic performance by modulating electronic coupling, creating active sites. Liu *et al.* designed Cu single-atom catalysts on N-doped TiO_2. The N dopants modulated d-p orbital coupling, which induced electron redistribution and enhanced the HER activity [80]. Tsang *et al.* found that N-doped TiO_2 in seawater benefited from an electrolyte-assisted polarization effect, extending carrier lifetime and achieving a 15.9% solar-to-H_2 efficiency (Fig. 3C) [81]. P doping primarily enhances photocatalytic H_2 evolution by synergizing with cocatalysts and optimizing H_2 adsorption energies. Sathish *et al.* loaded CoTe on P-doped g-C_3N_4, achieving a high HER rate due to CoTe's excellent conductivity and favorable H_2 adsorption energy [60]. S doping enhances photocatalytic performance through multiple mechanisms, including band structure modulation, alteration of surface hydrophilicity, and heterojunction formation, across various catalyst substrates. Ma *et al.* introduced S into g-C_3N_4, forming a heterojunction with $ZnIn_2S_4$ that achieved a high HER rate and 34.43% AQE, attributed to synergistic effects [82].

B doping enables synergistic optimization of catalytic performance through bulk-surface co-doping. Liu *et al.* synthesized B-doped TiO_2 with bulk and surface doping, which achieved a high HER rate without cocatalysts as bulk and surface B synergistically created active sites and suppressed recombination [83]. C doping enhances performance by modulating π-electron density, introducing defects, and decoupling energy level sites. Shi *et al.* used carbon self-doping and nitrogen defects to prepare g-C_3N_4 nanosheets, where the carbon dopants mediated charge separation and prolonged carrier lifetime, achieving a very high HER rate [84]. O doping optimizes band structures and constructs spatially separated redox energy levels. It demonstrates prominent effects in carbon nitride materials. Xu *et al.* synthesized O-doped g-C_3N_4

nanotubes, where O and benzene rings collaboratively constructed spatially separated redox levels, improving charge separation and active sites [85]. Se doping induces dipole polarization with defects. Li *et al*. designed Se-doped ZnCdS with sulfur vacancies, which generated a polarization field and optimized charge separation, achieving a high and stable HER rate (Fig. 3D) [86].

Non-metal doping achieves multiple enhancements through atomic substitution, defect introduction, or chemical bond formation. These effects include bandgap narrowing, charge separation enhancement, and surface property optimization such as hydrophilicity and adsorption energy. This strategy benefits from readily available precursors and mild preparation methods, including thermal polymerization or solvothermal synthesis. It has been applied in a wide range of materials, including carbon nitrides, oxides, and sulfides. However, non-metal atoms (*e.g.*, P, Se) often have atomic radii significantly different from those of the host atoms. This difference results in low substitution efficiency and the formation of localized defect clusters. Some non-metals are prone to oxidation and loss in oxidative environments, which can lead to structural collapse of the catalyst. Nevertheless, due to its low cost, abundant availability, mild synthesis conditions, and versatile tunability, non-metal doping holds promising potential for industrial applications if preparation and stability challenges are addressed.

3.3. Co-doping

Co-doping with multiple elements overcomes the intrinsic limitations of single-element doping, which often improves only part of a photocatalyst's performance. However, it fails to simultaneously address the multi-step bottlenecks of light absorption, charge separation, and surface reaction kinetics. By combining two or more dopants, co-doping enables synergistic tuning of the electronic structure. This approach facilitates the creation of active sites and the optimization of interfacial properties, thereby achieving multi-objective enhancement. Different co-doping combinations may offer unique advantages through mechanisms such as charge compensation, defect cooperation, and the formation of dual active sites.

Li *et al*. co-doped Rh and La into perovskite nanosheets, where Rh introduced charge-trapping sites and La provided charge compensation [87]. This synergy created a narrow active window, increasing the HER rate significantly. Hu *et al*. synthesized a composite with Co/N-doped carbon supporting $ZnIn_2S_4$ [88]. The Co-N moieties and Co nanoparticles acted as dual active sites for the HER and oxidation, enabling directional charge migration and greatly enhancing H_2 evolution rates and selectivity. Chen *et al*. designed W/S co-doped BiOI, where S introduced oxygen vacancies and improved hydrophilicity, while W provided rapid electron channels (Fig. 3E) [89]. The material achieved a high visible-light HER rate and excellent stability. Jiang *et al*. developed N/S co-doped g-C_3N_4 guided by density functional theory (DFT), which predicted an ideal H adsorption energy (Fig. 3F). The synthesized material showed high specific surface area and efficient charge transport, achieving a high HER rate [90].

Co-doping leverages the complementary functions of two or more elements to simultaneously overcome bottlenecks in light absorption, charge separation, and surface reactions, achieving a synergistic performance enhancement. Overall, the advantage of co-doping lies in its ability to simultaneously regulate light absorption, carrier dynamics, and surface reaction pathways. However, controllability, reproducibility, and scalable synthesis remain key challenges for future development.

In summary, heteroatom doping provides a powerful and multifunctional approach for engineering photocatalyst properties. This includes both single or multiple elements doping. The choice of dopant is a strategic decision that requires a balance between performance enhancement and practical constraints, such as cost, stability, and synthetic complexity. While single-element doping offers a direct route to modify specific properties, its limitations often become apparent when addressing the multifaceted requirements of overall water splitting systems. Co-doping emerges as a more holistic strategy to overcome these limitations. It promotes the synergistic optimization of light absorption, charge separation, and surface reaction kinetics. Future research should combine advanced computational screening with precise synthetic control to design the next generation of doped photocatalysts, moving beyond serendipitous discoveries toward rational design, with particular focus on long-term durability and scalability.

4. Functional group modification

Functional group modification introduces specific chemical groups onto the catalyst surface or framework to achieve multi-dimensional improvements, such as regulating electronic structure, optimizing interface properties, and constructing active sites. This strategy offers advantages, including high targeting precision, low modification cost, and high structural tunability.

4.1. Hydroxyl (-OH) functional group modification

Hydroxyl (-OH) groups are common hydrophilic functional groups that enhance photocatalytic H_2 evolution primarily by improving catalyst-water contact and increasing charge carrier separation efficiency. Cao *et al*. prepared -OH-modified $SrTiO_3$ (OH-STO) (Fig. 4A), where the superhydrophilicity accelerated water contact and the increased oxygen vacancy content promoted charge carrier separation [91]. The material achieved a piezophotocatalytic H_2 evolution rate of 701.2 μmol h^{-1} g^{-1}, 5.3 times higher than that of pure $SrTiO_3$ under photocatalytic conditions. Liu *et al*. constructed a surface carbon-coupled hydroxyl structure by reacting formaldehyde with unsaturated carbon atoms in g-C_3N_4 (Fig. 4B), resulting in an 11.18-fold enhancement in H_2 evolution efficiency [92]. This improvement originated from the enhanced H_2O adsorption capacity and the improved migration efficiency of photogenerated charge carriers. Dong *et al*. confirmed *via* first-principles calculations that g-C_3N_4_OHQIII exhibited a narrowed bandgap of 2.55 eV, significantly reduced HER overpotential, and enhanced light absorption across 350–800 nm [93]. Xiang *et al*. introduced ethanol groups (-CH_2CH_2OH) at the edges of g-C_3N_4, where the hydroxyl groups served as electron donors, accelerating electron transfer to the active centers. This modification synergized with interlayer phosphate groups to enable rapid charge carrier transport, resulting in a H_2 evolution rate of 72.17 μmol/h for P-UCN–NA, which was 13.4 times higher than that of pristine g-C_3N_4 [94]. The -OH functionalization enhances the hydrophilicity of catalysts, alleviating the contact barrier between the catalyst and aqueous phase. Its electron-donating properties facilitate directional transport of photogenerated electrons and can synergize with oxygen vacancies, phosphate groups, and other functional sites. However, -OH groups are highly reactive and prone to substitution or sublimation under intense light or high-temperature conditions, leading to limited long-term stability. Excessive -OH modification can form disordered adsorption layers, which may hinder electron transfer to water molecules. Additionally, -OH often couples with oxygen vacancies, making it difficult to distinguish its independent contribution. Therefore, -OH functionalization is more suitable for short-cycle, high-activity catalysts, while long-term applications require further stabilization strategies.

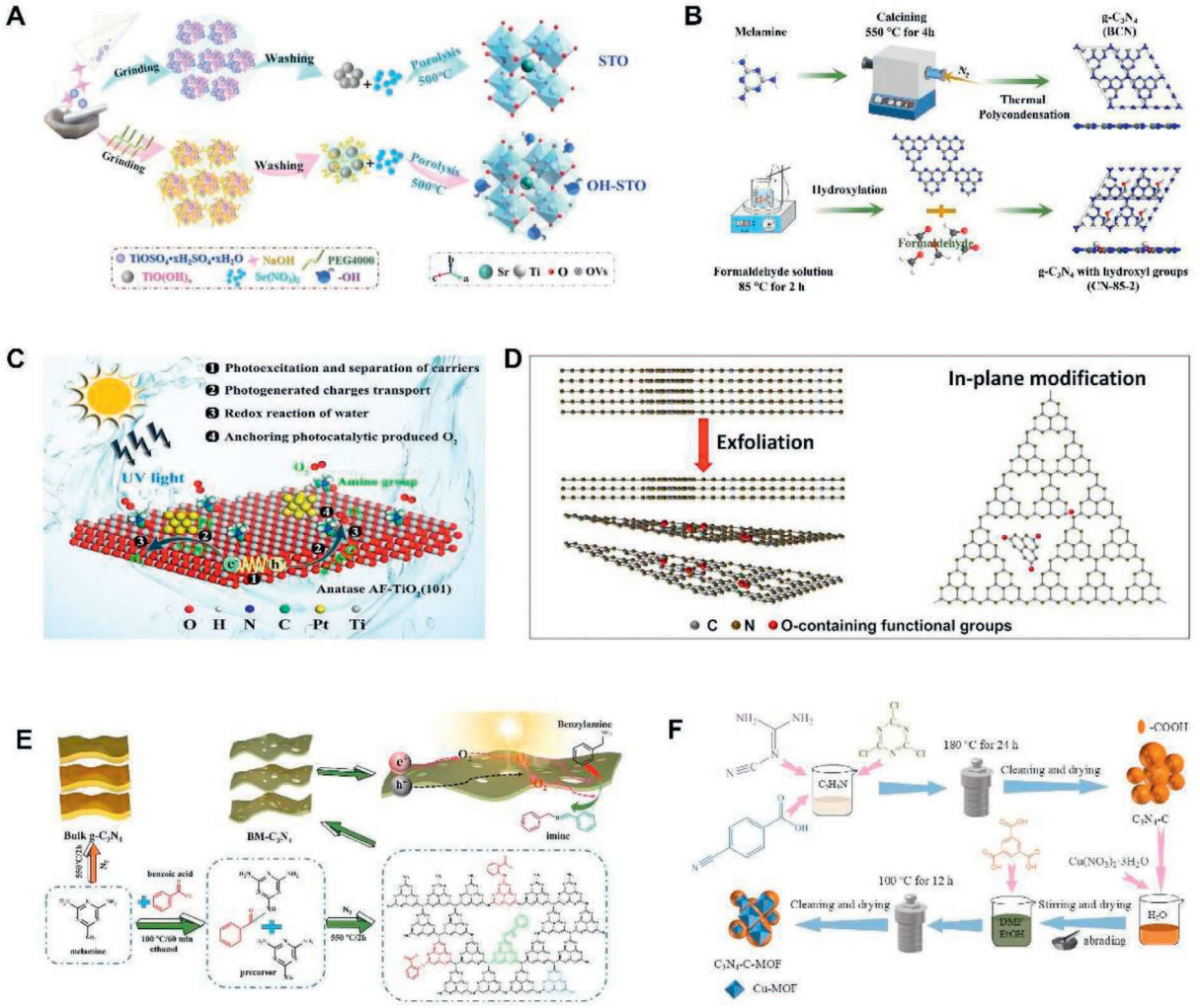


Fig. 4. Schematic illustration of representative functional-group modifications. (A) Schematic illustration of the preparation process of -OH-modified $SrTiO_3$. Reprinted with permission [91]. Copyright 2022, Elsevier. (B) Schematic illustration of the fabrication process of C-coupled hydroxylated g-C_3N_4. Reprinted with permission [92]. Copyright 2024, Royal Society of Chemistry. (C) Schematic illustration of the H_2 evolution mechanism of amine-functionalized TiO_2. Reprinted with permission [96]. Copyright 2022, Elsevier. (D) Schematic illustration of amino-group modification and the insertion of oxygen-containing functional groups on the surface of g-C_3N_4. Reprinted with permission [97]. Copyright 2023, Elsevier. (E) Schematic illustration showing how the introduction of benzoic acid brings hydroxyl and carboxyl groups, where these polar groups promote the formation of singlet oxygen and superoxide radicals. Reprinted with permission [100]. Copyright 2021, Elsevier. (F) Schematic illustration of the preparation of carboxylated g-C_3N_4. Reprinted with permission [101]. Copyright 2025, Elsevier.

4.2. Amino (-NH_2/-NH-) and amide (-CONH-) functional group modification

Amino functionalization enhances photocatalytic performance by providing lone-pair electrons to modulate surface metal centers, suppress H_2-O_2 recombination, or accelerate charge carrier transport. Qu *et al.* used ethylenediamine (EDA) as a modifier to coordinate N–Cu/Ni, linking Cu-In-Zn-S (CIZS) with NiSx to construct molecular bridges that facilitate charge transfer, achieving a H_2 evolution rate of 65.93 mmol g^{-1} h^{-1}, a new record for CIZS-based catalysts [95]. Wang *et al.* prepared amino-functionalized TiO_2 (AF-TiO_2) (Fig. 4C), where surface amide functional groups anchored O_2 and suppressed H_2-O_2 recombination [96]. The H_2 evolution activity of AF-TiO_2/Pt was 14.25 times higher than that of TiO_2/Pt. Guo *et al.* introduced abundant amino and oxygen-containing groups into g-C_3N_4 (Fig. 4D) *via* rapid high-temperature hydrothermal post-treatment, increasing H_2 evolution activity by 5.1 times due to enlarged surface area and improved charge-carrier separation [97]. Yao *et al.* incorporated pyridine rings (containing amino-derived structures) into carbon nitride to construct a quaternary homojunction. The electron-withdrawing effect of conjugated heterocycles triggered framework delocalization, achieving a H_2 evolution rate of 6.64 mmol g^{-1} h^{-1} with an AQE of 12.27 % at 420 nm [98]. Overall, amino functional group modification can regulate the electron density of metal active centers *via* the lone-pair electrons of amino groups, construct molecular bridges to facilitate interfacial electron transfer, and modulate surface adsorption behavior to suppress H_2-O_2 recombination. Inhibiting H_2-O_2 recombination is a key challenge in overall water splitting. Amino modification is suitable for systems that require rapid electron transfer, but it must be precisely matched to the material's band structure to avoid side effects.

4.3. Carboxyl (-COOH) and ester (-COOR) functional group modification

Carboxyl groups enhance performance through electron withdrawal/donation effects, π-conjugation extension, and interface optimization. Jiang *et al.* introduced 1,4-benzenedicarboxylic acid into the edges of polymeric carbon nitride (PCN), leveraging the synergistic effect of electron-withdrawing carboxyl groups and extended π-conjugation domains [99]. The H_2 evolution

rate of PCN-2AA-3 reached 1692.1 μmol g^{-1} h^{-1}, 3 times higher than that of pristine PCN, with an AQE of 16.4% at 420 nm. Dong *et al*. demonstrated theoretical calculations showing that g-C_3N_4-(OHQI+COOHQIII) possesses a narrow bandgap (2.39 eV) and strong light absorption, thereby significantly lowering the HER overpotential [93]. Hu *et al*. synthesized carboxyl-containing PCN *via* self-assembly of benzoic acid and melamine (Fig. 4E), where carboxyl groups promoted singlet oxygen generation while modulating heptazine units to enhance charge migration, indirectly improving H_2 evolution activity [100]. Yang *et al*. constructed a C_3N_4–C-MOF composite photocatalyst by grafting 4-carboxybenzoic acid onto g-C_3N_4 (Fig. 4F) and supporting a Cu-MOF. The H_2 evolution rate reached 12.68 mmol g^{-1} h^{-1}, which was 1.68 times higher than that of the non-carboxylated system. This enhanced performance is primarily attributed to the carboxyl groups, which strengthen interfacial interactions and improve charge separation efficiency [101].

4.4. Sulfonyl (-SO_2) and thiol (-SH) functional group modification

Sulfur-containing functional groups primarily enhance the separation efficiency of photogenerated electron-hole pairs and provide active sites. Huang *et al*. designed a non-fused sulfonyl-functionalized polymer, P-2SO_2 (Fig. 5A), in which flexible sulfur segments improved hydrophilicity and π-π stacking interactions [102]. The material achieved a H_2 evolution rate of 1060.1 μmol/h with an AQE of 32.4% at 460 nm, representing a 237% improvement over the control sample. Ma *et al*. functionalized Zr-MOF using thioglycolic acid (containing -SH) (Fig. 5B), enabling precise loading of CdS to form Zr-MOF-S@CdS. The H_2 evolution rate reached 1861.7 μmol g^{-1} h^{-1}, 4.5 times higher than that of pure CdS [57]. Zhang *et al*. introduced thiophene rings (sulfur-containing conjugated structures) and nickel complexes into CN. The TCN–NiL sample achieved a H_2 evolution rate of 136.7 μmol/h, five times higher than that of 3 wt% Pt/CN, with its photoresponse extended to 550 nm [103]. Yuan *et al*. functionalized boron nitride sheets (BNs) membranes with sulfonated CNF (-SO_3H, an acidic group similar to carboxyl), achieving a H_2 evolution rate of 13.97 μmol g^{-1} h^{-1}, attributed to efficient regulation of the hydrogen-bonding network of water molecules [104].

4.5. Fluoro (-F) and methyl (-CH_3) functional group modification

Halogen and alkyl groups enhance performance through electrostatic modulation, band structure optimization, and extended charge carrier lifetime. Gao *et al*. prepared CH_3@C_{60}/ZrS_2 and F@qHP-C_{60}/GeC heterojunctions [105]. The -CH_3 and -F groups enhanced surface electrostatic potential, reduced the Gibbs free energy of HER/OER, narrowed the bandgap to extend charge carrier lifetime, and strengthened Z-scheme charge separation. Xu *et al*. modified two-dimensional black phosphorus using the electronic effects of organic functional groups [106]. The -F (electron-withdrawing) and -CH_3 (electron-donating) groups modulated band edge positions by altering orbital occupation, significantly enhancing the visible-light H_2 evolution rate (Fig. 5C). Baek *et al*. reported that triazatruxene-based PPN with hexyl groups (-C_6H_{13}) facilitated electron transfer from donor to acceptor (Fig. 5D), enabling stable H_2 evolution in TATR-PPN [107].

4.6. Donor-acceptor (D-A) molecules, phenyl (-pH) functional group and phosphate group modification

D-A molecules and π-conjugated units achieve efficient regulation through directional charge migration and extended light absorption. Wu *et al*. synergistically modified CN using non-covalent π-π stacking (Fig. 5E) and covalent Schiff base condensation [108]. The D-A molecules simultaneously enhanced light absorption and promoted out-of-plane/in-plane charge transport, achieving a H_2 evolution rate of 41.71 mmol h^{-1} g^{-1}. Li *et al*. reported that fluorenone-based COF with phenyl group (electron-donating) functionalization (Fig. 5F) increased the H_2 evolution rate of FOOPh-COF to 228.5 mmol g^{-1} h^{-1}, 11.8 times higher than Br-functionalized (electron-withdrawing) FOOBr-COF [109]. This enhancement originated from the increased electron density at the CO active centers. Surface modification with phosphate related functional groups has been demonstrated as an effective strategy to enhance photocatalytic H_2 evolution. Zou *et al*. introduced phosphate species or phosphorus containing functional groups onto g-C_3N_4, which enhanced visible light absorption, improved charge separation, and strengthened interactions with Pt cocatalysts, resulting in a significantly increased H_2 evolution rate [110]. Li *et al*. employed a phosphorylation strategy using aminotris(methylenephosphonic acid) (ATMP) to modify g-C_3N_4, which facilitated liquid phase proton transfer and interfacial charge separation, enabling more efficient proton delivery to active sites and ultimately boosting photocatalytic H_2 evolution performance [111]. Although phosphate group modifications significantly enhance radical production and proton transfer, their efficacy remains highly sensitive to the specific nature of the reaction substrates, as the induced electrostatic field may competitively inhibit the adsorption of strongly binding species and hinder direct hole oxidation pathways.

In summary, functional group modification provides a versatile and powerful chemical toolkit for the surface and interface engineering of photocatalysts. The choice of functional groups determines the primary mechanisms of enhancement, ranging from increased hydrophilicity to guided charge transport. The optimal strategy depends on the specific constraints of the host material and the desired functionality. For instance, in large-scale overall water splitting, synergistic modification with hydroxyl groups (low-cost, highly hydrophilic) and amino groups (charge-bridging) is preferred. For high-salinity systems such as seawater, a combination of fluorine (salt-resistant) and hydroxyl groups can balance hydrophilicity and salt tolerance. When targeting high activity under laboratory conditions, D-A molecules and π-conjugated units are optimal, though cost and stability issues must be carefully considered. The redox stability of the functional groups, as well as the development of simpler and more scalable modification pathways, is critical for translating these promising strategies from laboratory research to practical applications.

5. Defect engineering

Defect engineering modulates the electronic structure and surface properties of catalysts. Different types of defects, including sulfur vacancies, oxygen vacancies, nitrogen vacancies, and their synergistic effects with doping and heterostructure construction, can significantly enhance photocatalytic H_2 evolution performance.

5.1. Anion/cation vacancy defect systems

Anion vacancy defect systems, centered on vacancies of sulfur, oxygen, nitrogen, phosphorus, and other anions, enhance photocatalytic H_2 evolution performance by modulating the electronic structure of catalysts, exposing active sites, and optimizing interfacial interactions. They are among the most extensively studied systems in defect engineering.

In the sulfur vacancy subcategory, Jin *et al*. synergistically modulated the surface state of MoS_2 through sulfur vacancies and oxygen atom doping, constructing an H-GDY/O-MoS_{2-x} Type II heterojunction (Fig. 6A). The sulfur vacancies increased the interfacial potential difference, achieving a H_2 evolution rate of 2272.97 μmol g^{-1} h^{-1}, which was 25 times higher than that of pure MoS_2 [112].

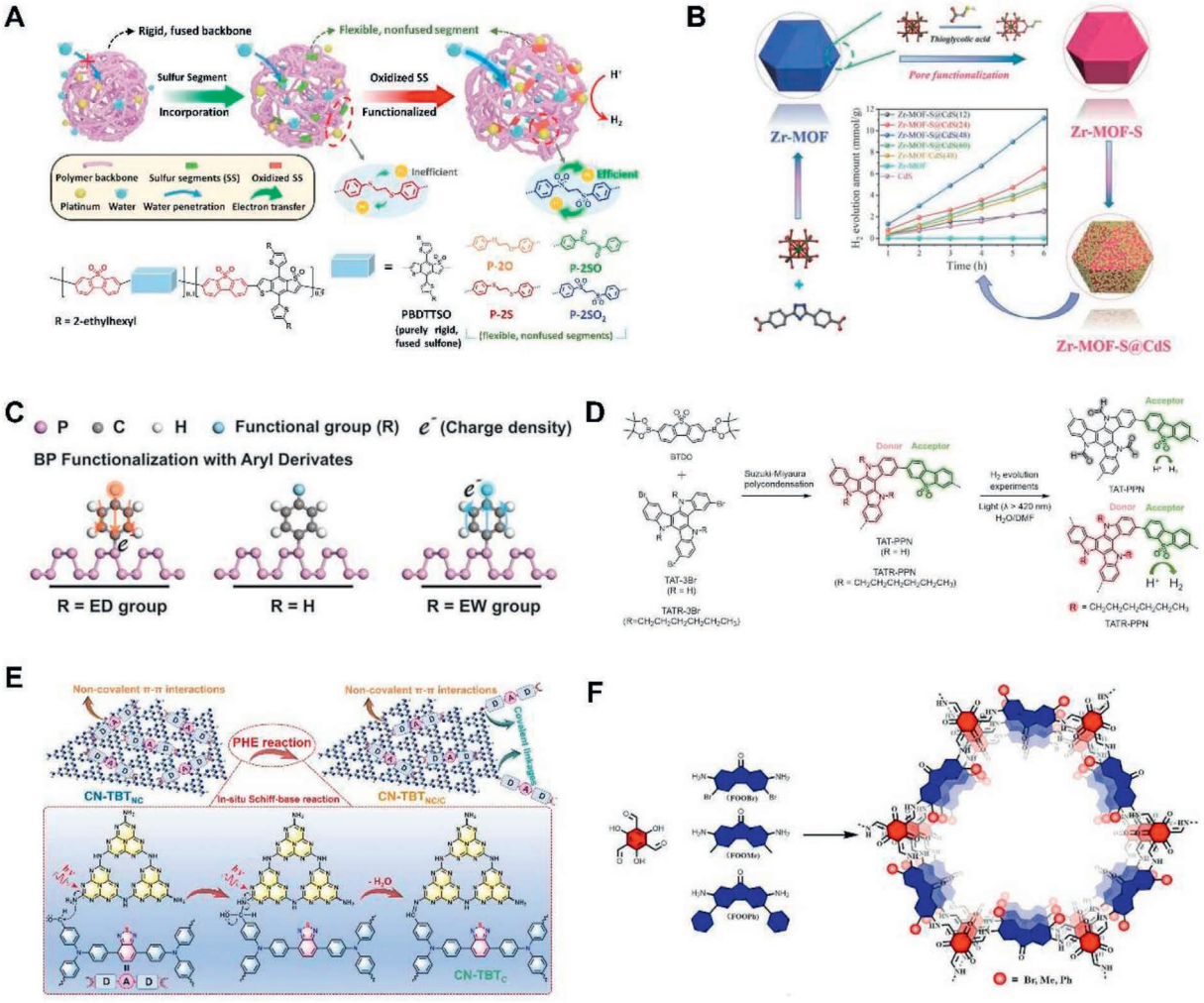


Fig. 5. Schematic illustration of representative molecular and polymer functionalization strategies. (A) Schematic illustration of introducing non-melting flexible sulfur segments (SSs) into a polymer backbone to enhance hydrophilicity and accessibility of active sites. Reprinted with permission [102]. Copyright 2025, AAAS. (B) Schematic illustration of MOF surface functionalization using thioglycolic acid. Reprinted with permission [57]. Copyright 2022, Elsevier. (C) Schematic illustration of organic functional-group modification of two-dimensional black phosphorus. Reprinted with permission [106]. Copyright 2024, John Wiley and Sons. (D) Schematic illustration of the porous polymer network structure modified with hexyl groups. Reprinted with permission [107]. Copyright 2024, John Wiley and Sons. (E) Schematic illustration of a CN photocatalyst incorporating donor-acceptor (D-A) molecular units. Reprinted with permission [108]. Copyright 2025, Elsevier. (F) Schematic illustration of COFs functionalized with phenyl groups. Reprinted with permission [109]. Copyright 2024, Elsevier.

Chen *et al.* utilized sulfur vacancies to stabilize Pt single atoms confined on the surface of $CdIn_2S_4$ [113]. The resulting Pt_1/CISv catalyst exhibited a H_2 evolution rate 12 times higher than that of pure $CdIn_2S_4$. Xie *et al.* loaded $CoNi_2S_4$ onto the surface of CdS containing sulfur vacancies (Fig. 6B), where the sulfur vacancies enhanced the built-in electric field of the Schottky junction. The 30 % $CoNi_2S_4$/VsCdS achieved a H_2 evolution rate as high as 76.93 mmol g^{-1} h^{-1} [114]. Overall, sulfur vacancies can significantly enhance electron mobility and the interfacial electric field strength in chalcogenides. However, their thermal stability is relatively poor, and under prolonged illumination, they are prone to migration or aggregation, leading to performance degradation. This limits their long-term operational stability under intense light conditions. In the oxygen vacancy subcategory, Hota *et al.* introduced oxygen vacancies into CeO_2 *via* chemical etching, thereby forming an MCO-X heterojunction that switched the charge transfer mechanism from Type I to Type II. The MCO-30 sample achieved a H_2 evolution rate of 3286.2 μmol h^{-1} g^{-1} [115]. Jin *et al.* prepared a composite catalyst comprising Ov-$NiCo_2O_4$ and ZnCdS, in which oxygen vacancies enhanced H_2 evolution performance by 3 times compared to the defect-free sample [116]. Chen *et al.* prepared a Pd-TiO_2_Ov catalyst (Fig. 6C). Oxygen vacancies enabled a photocatalytic hydrogenation yield of 99.9 %, significantly surpassing the 74 % achieved with pure TiO_2 loaded with Pd [117]. The advantage of oxygen vacancies lies in their versatile tunability and high stability in metal oxides. However, the broad defect states they introduce can enhance electron-phonon interactions, leading to a degree of thermalized electron loss in the catalyst, particularly under high-temperature conditions.

The nitrogen vacancy subcategory primarily focuses on carbon nitride materials. Dong *et al.* developed a nitrogen-defective carbon nitride supported Pt single atom catalyst, where nitrogen vacancies reduced the exciton binding energy from 86.92 meV to 43.20 meV, increasing the H_2 evolution rate by 41 times [118]. Wan *et al.* synthesized C_3N_4_ND, which synergized N_1 vacancies and cyano groups to achieve a H_2 evolution rate of 39.18 mmol g^{-1} h^{-1} in a TEOA system, 75.34 times higher than that of bulk C_3N_4 [119]. Wong *et al.* prepared nitrogen-deficient g-C_3N_4 *via* rapid Joule heating; after Pt loading (Fig. 6D), the H_2 evolution rate reached 16,936.5 μmol h^{-1} g^{-1} [120]. Nitrogen vacancies significantly promote exciton dissociation in g-C_3N_4-based materials, but in most studies, structural damage to the carbon framework is difficult to avoid, resulting in reduced crystallinity in some samples. Therefore, maintaining the integrity of the framework while introducing nitrogen vacancies remains a key challenge for future research.

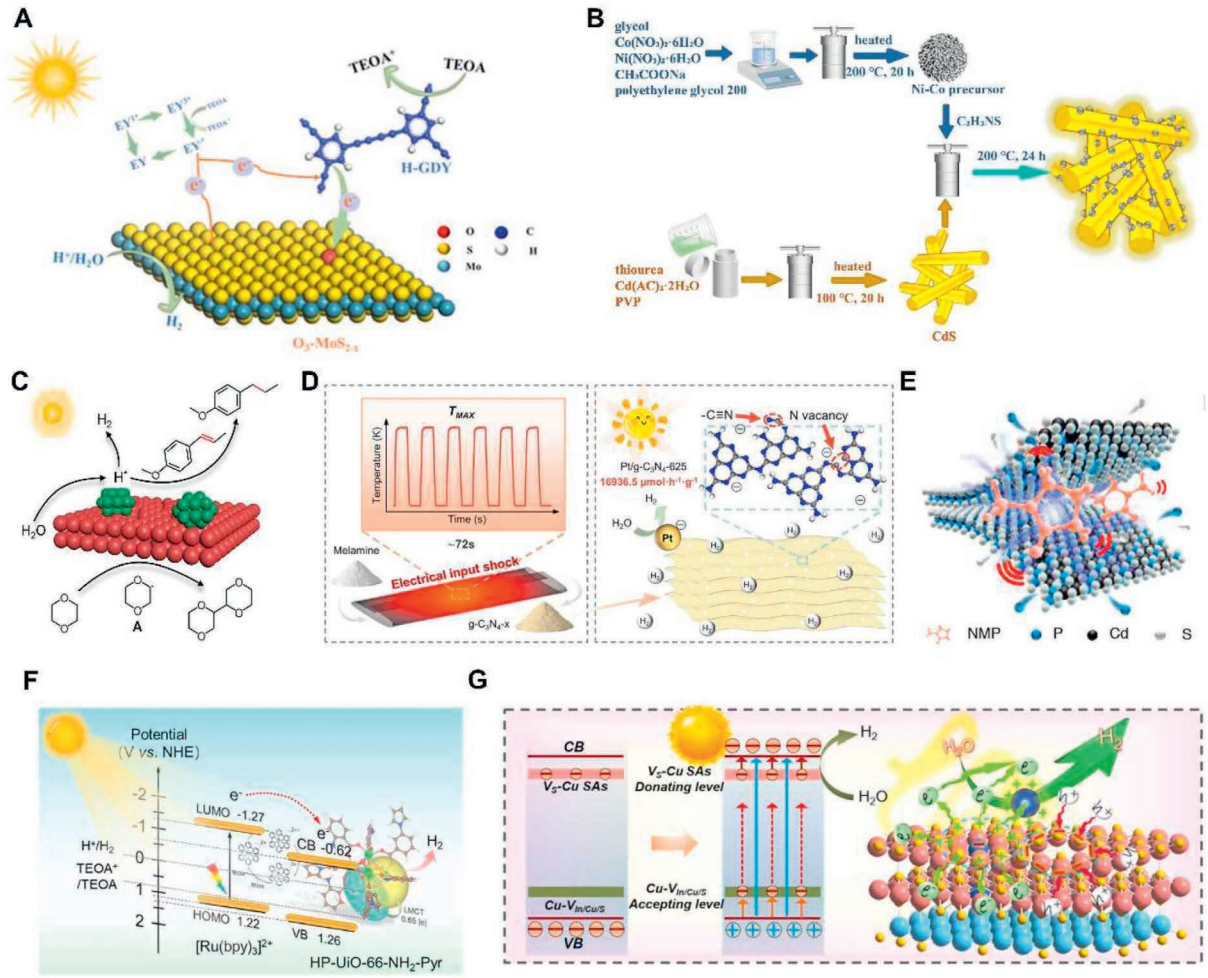


Fig. 6. Schematic illustration of representative studies on sulfur-vacancy and related defect engineering. (A) Schematic illustration of surface modulation of MoS_2 through the synergistic effects of sulfur vacancies and oxygen doping. Reprinted with permission [112]. Copyright 2025, Elsevier. (B) Schematic illustration of $CoNi_2S_4$ loaded onto CdS with introduced sulfur vacancies. Reprinted with permission [114]. Copyright 2025, Elsevier. (C) Schematic illustration of Pd-loaded TiO_2 with oxygen vacancies. Reprinted with permission [117]. Copyright 2025, KeAi Publishing. (D) Schematic illustration of the preparation of layered mesoporous nitrogen-deficient g-C_3N_4. Reprinted with permission [120]. Copyright 2025, John Wiley and Sons. (E) Schematic illustration of the defect-rich $CdPS_3$ nanosheets containing sulfur and phosphorus vacancies. Reprinted with permission [122]. Copyright 2025, John Wiley and Sons. (F) Schematic illustration of photoinduced charge transfer in the HP-UiO-66-NH_2-Pyr photocatalyst prepared through Zr-site vacancy creation and Clausen-Kaas-mediated pyridone functionalization. Reprinted with permission [124]. Copyright 2025, John Wiley and Sons. (G) Schematic illustration of the catalytic mechanism of $ZnIn_2S_4$ with Cu/In/S multi-vacancies. Reprinted with permission [125]. Copyright 2024, Elsevier.

The phosphorus vacancy subcategory shows significant research potential. In Zhu *et al.*, a CoP-Vp@CZS catalyst was prepared; phosphorus vacancies adjacent to Co atoms mediated electron transfer, increasing the H_2 evolution rate by 14.66 times compared with pure $Cd_{0.5}Zn_{0.5}S$ [121]. Wang *et al.* developed a S/P dual-defective $CdPS_3/ZnIn_2S_4$ hybrid (Fig. 6E), where phosphorus and sulfur vacancies synergistically constructed intermediate energy levels, resulting in a H_2 evolution rate 4.45 times higher than that of pure $CdPS_3$ [122]. Dai *et al.* revealed the dual role of intrinsic phosphorus vacancies in red phosphorus: deep-level charge trapping by phosphorus vacancies leads to loss of active electrons, while oxygen doping to fill the vacancies eliminates harmful defect states, prolongs free electron lifetime, and enhances H_2 evolution performance [123].

Cation vacancy defect systems primarily involve missing metal cation sites in the catalyst, which optimize the local environment of metal active centers and regulate charge transport pathways. Han *et al.* constructed Zr site vacancies in UiO-66 *via* defect engineering, followed by pyrrole functionalization to prepare an HP-UiO-66-NH_2-Pyr catalyst (Fig. 6F). The Zr vacancies and pyrrole conjugation synergistically optimized the Zr-O cluster microenvironment, reducing charge carrier recombination and extending electron lifetime and migration rate. The H_2 evolution rate reached 4831.7 $\mu mol\ g^{-1}\ h^{-1}$, over 10 times higher than that of pure UiO-66-NH_2 [124]. Li *et al.* prepared RCu-ZIS catalysts, where Cu/In/S vacancy clusters were contained in cation vacancies (Fig. 6G). These vacancies, in combination with Cu^+ doping and Cu single atoms, generated a local electric field that accelerated charge-carrier separation. The H_2 evolution rate reached 70.58 $mmol\ g^{-1}\ h^{-1}$ [125], with In cation vacancies playing a critical role in charge localization and active site construction. The unique advantage of cation vacancies lies in their ability to directly modulate the electron density and coordination environment of metal active centers in catalysts. Cation vacancies can directly modulate the metal active centers, which is their unique advantage; however, they may also disrupt the metal-ligand framework, leading to structural collapse. Future work should aim to find a dynamic balance between high defect concentration and structural stability.

In summary, both anion and cation vacancy systems generally enhance charge separation efficiency and interfacial reaction kinetics, but they still have limitations. Precise defect control is

challenging, deep-level defects may act as recombination centers, and high defect concentrations can compromise structural stability. Therefore, future research should integrate *in situ* characterization techniques and theoretical calculations to achieve atomically controlled defect design.

5.2. Heteroatom doping-induced defect systems

Heteroatom doping-induced defect systems introduce heteroatoms with significant differences in atomic radius or electronegativity relative to the host lattice, thereby inducing lattice distortion and generating defects to regulate electronic structure and optimize performance. The doped atoms and the induced defects act synergistically.

In carbon nitride systems, Lai *et al.* prepared S self-doped carbon nitride (SCN) *via* thermal polymerization. Sulfur doping stimulated electron delocalization at active sites while inducing defects that interact with cyano groups [126]. The H_2 evolution rate of SCNV reached 3437 μmol g^{-1} h^{-1}, three times higher than SCN. In another study by Lai *et al.*, S-modified dual-defective g-C_3N_4 (SDCN) was developed, in which C-S-C bonds optimized electronic pathways [127]. The synergy between defects and doping enhanced the H_2 evolution rate to 1613.5 μmol g^{-1} h^{-1}, 31.5 times higher than that of pure MCN. Lv *et al.* simultaneously introduced oxygen doping and nitrogen vacancies into g-C_3N_5, with Pt single atoms anchored *via* Pt-N_3 bonds, thereby enriching electrons around N atoms [128]. The H_2 evolution rate of Pt SAs/g-C_3N_{5-x}-O was 119 times higher than that of pure g-C_3N_5.

In sulfide systems, Jin *et al.* reported H-GDY/O-MoS_{2-x} catalysts, in which oxygen doping and sulfur vacancies synergistically formed heterojunctions, modulating the band structure and enhancing the driving force for electron transfer [112]. Zheng *et al.* prepared hydrogen-doped TiO_2 (H-TiO_2), in which H atoms substituted for O atoms to form Ti-H bond defects, which could be converted to oxygen vacancies *via* annealing [129]. Both types of defects enhanced visible light absorption. The H_2 evolution activity was 60 times higher than that of commercial rutile TiO_2.

5.3. Composite defect systems

Composite defect systems are catalysts containing two or more types of defects (or defects combined with other modification strategies), in which synergistic interactions between defects overcome the performance limitations of single-defect systems. These systems excel at generating local electric fields, extending the light absorption range, and optimizing the distribution of active sites.

Synergy between dual anion vacancies: Zhang *et al.* reported MSv/ZISv catalysts containing dual sulfur vacancies in MoS_2 and $ZnIn_2S_4$, which promoted charge carrier separation *via* electron redistribution and defect-state construction [130]. The H_2 evolution rate reached 8.83 mmol g^{-1} h^{-1}, which was 21.91 times higher than pure $ZnIn_2S_4$. Xu *et al.* prepared H–CeO_2/H–CdS core-shell spheres with both oxygen and sulfur vacancies, which jointly modulated the electronic structure and extended light absorption to the visible-near-infrared region, improving CdS photostability [131].

Synergy between defects and heterojunctions: Li *et al.* prepared HVs-ZIS/CIS heterojunctions incorporating defects in $ZnIn_2S_4$ to introduce intermediate energy levels, and strong interfacial coupling enhanced the built-in electric field [132]. The H_2 evolution rate reached 33.65 mmol g^{-1} h^{-1}.

Synergy between defects and single atoms: Lv *et al.* prepared Pt SAs/g-C_3N_{5-x}-O, in which Pt single atoms synergized with nitrogen vacancies and oxygen doping to lower the H^* formation energy barrier [128]. Li *et al.* prepared CuS@ZnS, which triggered a PIDCT mechanism *via* interfacial defects, enabling efficient utilization of infrared light [133]. Zong *et al.* prepared a PbS/MoS_x/perovskite system, in which defect passivation by PbS was combined with catalysis by MoS_x, achieving an STC efficiency of 4.63 % [134]. These examples collectively demonstrate the diversified advantages of composite defect systems.

Heteroatom doping and defect engineering exhibit synergistic effects: the dopant atoms modulate the band structure, while the induced defects act as charge traps, together achieving the dual objectives of enhanced light absorption and accelerated charge separation. The type and concentration of the resulting defects are sensitive to the dopant characteristics, concentration, and synthesis conditions, making the system difficult to optimize rationally and reproduce reliably. There is a risk of creating over-engineered systems with excessive disorder and a wide range of defect types, leading to unpredictable electronic structures and potential conflicts between different modification mechanisms. Future work should establish a unified theoretical framework for band structure regulation to enable predictable materials design.

6. Heterostructure construction

Heterojunction engineering optimizes photocatalytic H_2 evolution performance by establishing interfacial contacts between two or more semiconductors/conductors, leveraging mechanisms such as band structure matching, built-in electric-field regulation, and interfacial charge transfer. In recent years, multiple heterojunction types such as S-scheme, Z-scheme, and Schottky junctions have been extensively developed [135,136]. By precisely controlling charge transfer pathways, retaining strong redox properties, and increasing active site density, these heterostructures significantly enhance photocatalytic H_2 evolution performance.

6.1. S-scheme heterojunction systems

S-scheme heterojunctions achieve spatial separation of photogenerated electron-hole pairs while preserving the strong redox capabilities of both components by establishing appropriate band edge alignment and a strong internal electric field. Yu *et al.* constructed a rod-rod S-scheme heterojunction by self-assembling HOF with WO_3 nanorods [137]. The C–O-W coordination bonds promoted the formation of a strong internal electric field. Under 455 nm LED irradiation, the H_2 evolution rate reached 475.5 mmol g^{-1} h^{-1}, 2.7 times higher than that of pure HOF, and the activation energy decreased from 15.60 kJ/mol to 9.57 kJ/mol, significantly accelerating surface reaction kinetics (Fig. 7A). Wang *et al.* constructed a closely contacted ST@BTTA S-scheme heterojunction (Fig. 7B) by *in situ* growth of COF (BTTA) on the surface of a sponge-like TiO_2 [138]. DFT calculations confirmed its optimal adsorption-desorption capability for H_2O and H_2. The H_2 evolution rate of ST@BTTA-120 was 10.3 times and 2.6 times higher than those of pure ST and BTTA, respectively. XPS and ESR analyses verified the S-scheme charge transfer mechanism. S-scheme heterojunctions drive the recombination of low-energy electrons and holes *via* the built-in electric field while retaining high-energy charge carriers for surface reactions. Charge transfer can be further enhanced by introducing defects (intermediate energy levels) and by forming interfacial bonds (coordination or covalent). The key advantage of S-scheme heterojunctions over Type II heterojunctions is their ability to maximally preserve the strong oxidative and reductive capabilities of the oxidizing and reducing agents.

6.2. Z-scheme heterojunction systems

Z-scheme heterojunctions spatially separate photogenerated electrons and holes while preserving strong redox capabilities. Based on the charge transfer medium, they can be classified into

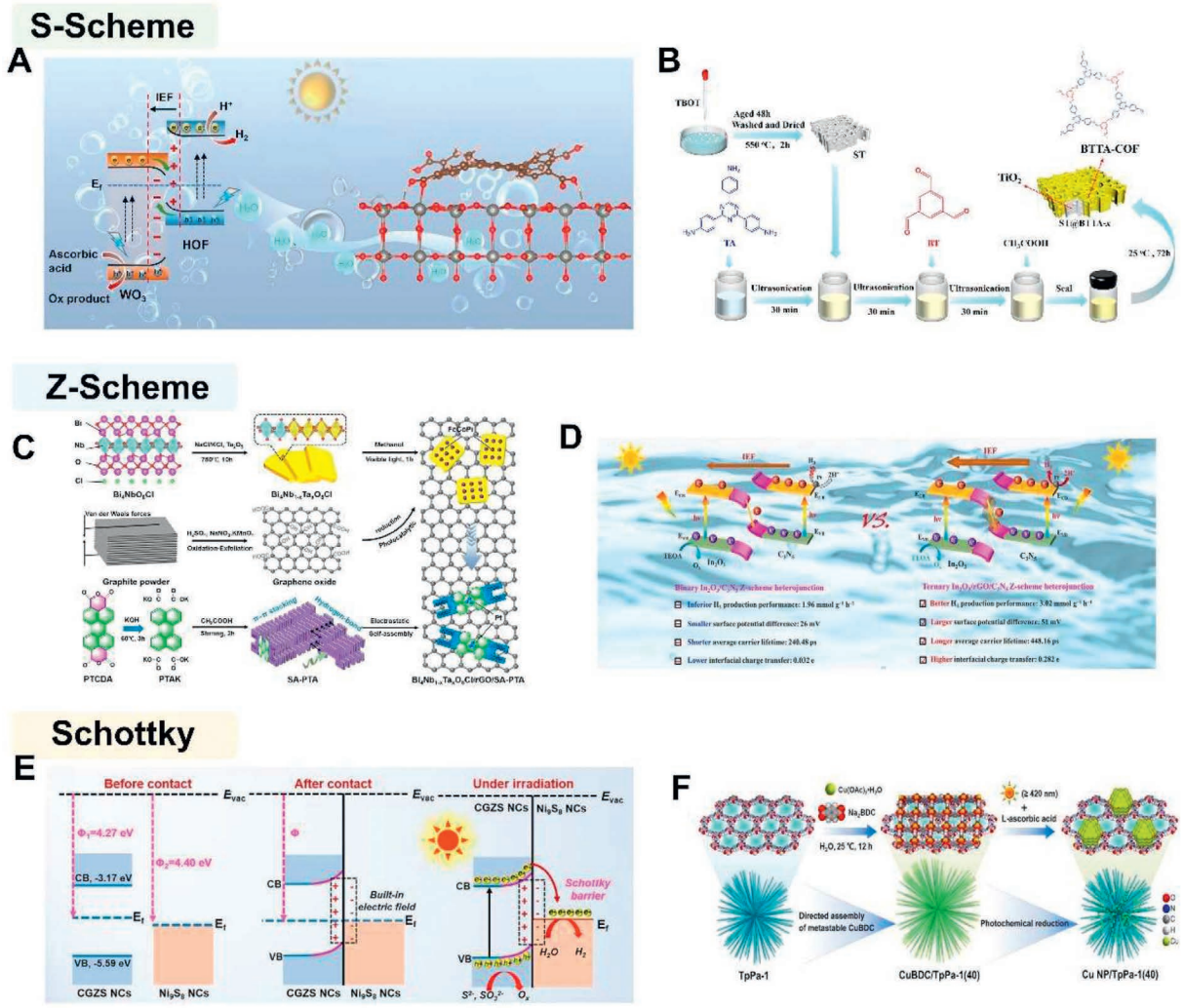


Fig. 7. Schematic illustration of representative studies on S-scheme heterojunctions. (A) Schematic illustration of a rod-rod-type S-scheme heterojunction (HOF-WO_3) constructed by tightly integrating HOF with WO_3 nanorods. Reprinted with permission [137]. Copyright 2025, Elsevier. (B) Schematic illustration of the preparation of a sponge-like TiO_2@BTTA S-scheme heterojunction with a tightly contacted interface. Reprinted with permission [138]. Copyright 2025, Elsevier. (C) Schematic illustration of the fabrication of an inorganic-organic $Bi_4Nb_{1-x}Ta_xO_8Cl$/rGO/SA-PTA Z-scheme heterojunction. Reprinted with permission [139]. Copyright 2025, American Chemical Society. (D) Schematic illustration of the photocatalytic mechanism of the In_2O_3/rGO/C_3N_5 Z-scheme photocatalyst. Reprinted with permission [140]. Copyright 2026, Elsevier. (E) Schematic illustration of the photocatalytic mechanism of CGZS/Ni9S8 Schottky heterojunctions. Reprinted with permission [143]. Copyright 2025, John Wiley and Sons. (F) Schematic illustration of binary Schottky heterojunctions composed of copper nanoparticles anchored on a COF. Reprinted with permission [144]. Copyright 2025, Elsevier.

direct Z-scheme, electron-mediated Z-scheme, and all-solid-state Z-scheme.

Direct Z-scheme heterojunctions require no additional medium and rely on interfacial electric fields to drive charge transfer. Fu *et al.* constructed an inorganic-organic $Bi_4Nb_{1-x}Ta_xO_8Cl$/rGO/SA-PTA Z-scheme heterojunction (Fig. 7C), where the mobile π-electrons of rGO coupled with the enhanced interlayer polarization of $Bi_4Nb_{1-x}Ta_xO_8Cl$ and the increased molecular dipole moment of SA-PTA, forming a three-stage polarization electric field composed of two built-in electric fields and one interfacial electric field [139]. This configuration enabled continuous charge transfer from OEP to HEP, increasing charge separation efficiency by 3.6 times and reducing the interfacial charge transfer time from 54.8 ps to 38.2 ps. The H_2 and O_2 evolution rates in overall water splitting were 5.2 times higher than those of $Bi_4Nb_{1-x}Ta_xO_8Cl$/SA-PTA.

Electron-mediated Z-scheme heterojunctions facilitate charge transfer through redox mediators or electron conductors. Zhang *et al.* constructed an In_2O_3/rGO/C_3N_5 ternary electron-mediated Z-scheme heterojunction (Fig. 7D), using rGO as an electron mediator. DFT calculations and Bader charge analysis indicated that rGO significantly enhanced the built-in electric field [140]. Femtosecond transient absorption spectroscopy showed that the average carrier lifetime (448.16 ps) was much longer than that of the direct Z-scheme In_2O_3/C_3N_5 system (240.48 ps). Under light irradiation, the surface potential difference reached 51 mV, twice that of the binary system (26 mV), and the H_2 evolution rate increased by 1.5 times. Ma *et al.* anchored Fe^{3+}/Fe^{2+} redox mediators on a COF skeleton to construct a TP1C/Bi_2WO_6 two-dimensional Z-scheme heterojunction, avoiding the instability and low transfer efficiency caused by mediator dispersion in conventional solutions [141]. The 25 % BWO/Fe/TP1C sample achieved a H_2 evolution rate of 6.31 mmol g^{-1} h^{-1}, which was 28.68 times higher than that of the pure COF and 2.3 times higher than that of the system without Fe mediators.

All-solid-state Z-scheme heterojunctions use conductive media to bridge interfaces, addressing the charge transfer bottlenecks of traditional Z-schemes. Zhang *et al.* constructed transition-metal nitride (TMN)-bridged all-solid-state Z-scheme heterojunctions, such as WO_3@W_2N/$ZnIn_2S_4$, *via* an *in situ* nitridation strategy [142]. The introduction of W_2N optimized charge transfer behavior and en-

hanced the built-in electric field. The WWZ system achieved a H_2 evolution rate of 8.9 mmol g^{-1} h^{-1}, which was 20 times and 9.5 times higher than those of pure $ZnIn_2S_4$ and $WO_3/ZnIn_2S_4$, respectively.

Z-scheme heterojunctions achieve spatial charge separation while maintaining high redox capability. They possess strong redox potentials, adapt to diverse reaction scenarios, and their charge transfer efficiency can be optimized through mediators. However, several challenges remain. The actual direction of electron flow at the interface is difficult to verify directly. Most Z-schemes rely on additional mediators, which may trigger reverse reactions. Interfacial recombination losses are often underestimated. In particular, conventional Z-schemes suffer from energy losses and poor long-term stability. Nevertheless, Z-schemes remain indispensable for overall water splitting, especially for the O_2 evolution half-reaction. However, their application scope must be clearly defined: They are suitable for systems that demand strong oxidation and reduction, rather than all photocatalytic scenarios.

6.3. Schottky heterojunction systems

Schottky heterojunctions facilitate unidirectional transfer of photogenerated electrons from the semiconductor to the metal *via* the Schottky barrier at the metal/semiconductor interface, thereby suppressing electron-hole recombination and enabling the metal to serve as active sites for H_2 evolution. Tang *et al*. constructed a colloidal Schottky heterojunction (Fig. 7E) between Ni_9S_8 nanocrystals and Cu-Ga-Zn-S (CGZS) nanocrystals [143]. Strong electronic coupling enabled the optimized CGZS/2.0 wt% Ni_9S_8 to achieve a H_2 evolution rate of 6.68 mmol g^{-1} h^{-1} under visible light, which was 3.6 times higher than that of pure CGZS. Ni_9S_8 not only accelerated electron extraction but also served as highly efficient active sites for H_2 evolution. Wang *et al*. anchored Cu nanoparticles to the surface of a COF *via* photochemical reduction (Fig. 7F), thereby forming a binary Schottky heterojunction [144]. The interfacial electronic synergy between Cu and the COF enhanced light absorption, shortened electron migration distance, and exposed more proton reduction sites. The H_2 evolution rate reached 16.89 mmol g^{-1} h^{-1}, which was 7.7 and 2.83 times higher than those of the physical mixture and Pt-based photocatalysts, respectively. Guo *et al*. designed a $Mn_{0.4}Cd_{0.6}S$ (MCS)/$Ni_{0.85}Se$ Schottky heterojunction, where the work function difference drove the directional electron transfer from MCS to $Ni_{0.85}Se$ [145]. The coordinatively unsaturated Ni sites on the $Ni_{0.85}Se$ surface preferentially adsorbed and dissociated H_2O molecules by optimizing the d-band center. Simultaneously, the adsorption-desorption energy barriers of H^* and OH^* were regulated, achieving a H_2 evolution rate of 42.5 mmol g^{-1} h^{-1}, which was 3.34 times higher than that of pure MCS. Jin *et al*. modulated the exposed crystal facets of Co_3O_4, enabling HCO (exposing the (111) facet) to form an Ohmic-Schottky composite heterojunction with $Cd_{0.5}Zn_{0.5}S$ (CZS) [146]. The synergistic effect of crystal anisotropy and the heterojunction reduced the Gibbs free energy of hydrogen adsorption, promoting spatial separation and rapid transfer of charge carriers. HCO/CZS exhibited the highest H_2 evolution activity among the investigated samples. The greatest advantage of Schottky heterojunctions lies in their interfacial barrier, which enables unidirectional electron flow, suppresses recombination, and provides a well-defined charge transfer mechanism. However, their performance is sensitive to the metal's work function, and excessive metal loading can lead to light-shielding effects and plasmon-induced side reactions.

6.4. Other heterojunction systems

Type II heterojunctions achieve spatial separation of electrons and holes by constructing a staggered band alignment, enabling the transfer of electrons and holes to the conduction band and valence band of the two components, respectively [147]. Molecular-scale organic heterojunctions form charge transfer channels through intermolecular interactions, enabling near-infrared light response. Tandem heterojunctions integrate two or more heterojunction types to construct a dual electron-hole consumption pathway, leveraging the synergistic effect of multiple built in electric fields to enhance charge separation efficiency further.

In Type II heterojunctions, Zhang *et al*. employed a dual-solvent strategy to uniformly load Ni_3S_4 or CoS_2 nanoparticles onto the surface of a porphyrin-based MOF (PCN-222(Zn)), constructing a Type II heterojunction [148]. The H_2 evolution activity of PCN-222(Zn)-Ni_3S_4 was 47 and 16 times higher than that of pure PCN-222(Zn) and nickel sulfide, respectively, with excellent cycling stability. Lan *et al*. constructed an NH_2−MIL-125(Ti)/TpBpy-COF Type II heterojunction by modulating the exposed crystal facets of the MOF [149]. After combining decahedral NH_2−MIL-125(Ti) with the COF, the overall water splitting under visible light achieved H_2 and O_2 evolution rates of 331.6 and 165.7 μmol g^{-1} h^{-1}, respectively, representing the best performance among COF-based catalysts to date. Crystal facet anisotropy significantly influenced the strength of the built-in electric field in the heterojunction. The advantage of Type II heterojunctions lies in their simple structure and general ease of construction. However, their drawback is a weakened oxidation and reduction capability, making them insufficient to drive overall water splitting. In addition, they require precise band alignment; even slight deviations can lead to energy loss or interfacial recombination. Therefore, Type II heterojunctions are more suitable as H_2 evolution structures in sacrificial-agent systems rather than for demanding overall water splitting applications without sacrificial agents.

In molecular-scale organic heterojunctions, Zhang *et al*. developed PBDB-T/BTPT-IC4F heterojunction nanoparticles, where molecular matching between the donor polymer and an A-D1-D2-D1-A type acceptor enabled effective extraction of photogenerated holes from the HOMO of BTPT-IC4F to the HOMO of PBDB-T [150]. Calculations confirmed that PBDB-T prolonged the excited-state lifetime of BTPT-IC4F, achieving a H_2 evolution rate of 12.77 mmol h^{-1} g^{-1} under visible-near-infrared light, with an external quantum efficiency (EQE) of 6.3 % at 730 nm. Zhu *et al*. self-assembled PTA and NDI into an NDI/PTA molecular-scale heterojunction *via* π-π stacking, forming a Z-scheme electron transfer pathway [151]. The strong intermolecular charge density distribution generated a significant dipole moment of 8.83 D and a strong built-in electric field of 148.90 mV. The H_2 evolution rate reached 45.59 mmol g^{-1} h^{-1}, 2.73 times that of pure PTA, with an excellent AQE at 450 nm. This type of system offers unique advantages, such as precise energy–level regulation and near–infrared responsiveness. It generally suffers from poor structural stability, difficulty in scaling up, and challenges in maintaining interfacial contact. Future work urgently needs breakthroughs in large-scale processability.

In tandem heterojunctions, Jin *et al*. designed an H-GDY/CdS/VSe-ZnSe ternary tandem heterojunction, constructing a series structure of a CdS/VSe-ZnSe Type II heterojunction and an H-GDY/CdS S-scheme heterojunction through selenium vacancy modification [152]. The built–in electric field drove directional charge transport. Electrons from the conduction band of CdS transferred to VSe–ZnSe for H_2 evolution, while holes from the valence band transferred to H–GDY and were consumed. This achieved efficient spatial separation of electrons and holes. The Zn monomers in VSe–ZnSe provided abundant active sites. H–GDY broadened the light absorption range. The optimized CVZH-15 catalyst achieved a H_2 evolution rate of 127.2 mmol/g, 66.9 times higher than that of unmodified CdS. Zhang *et al*. introduced Co dual atoms between $ZnIn_2S_4$ (ZIS) and g-C_3N_4 (SCN) layers *via* a thiol-assisted coordination strategy, constructing a dual Z-scheme

Table 2
Representative performances for water splitting.

Catalyst	Modification strategy	Light source	H_2 evolution rate	Ref.
Pt-doped Cs_2SnBr_6	Noble metal doping	Visible light	11.49 mmol g^{-1} h^{-1}	[74]
Mn^{2+}-doped $ZnIn_2S_4$	Transition metal doping	420 nm (with magnetic field applied)	32.75 mmol g^{-1} h^{-1}	[75]
N-doped TiO_2	Non-metal doping	575–850 nm	40 mmol g^{-1} h^{-1}	[81]
W/S co-doped BiOI	Co-doping	460 nm	9.46 mmol g^{-1} h^{-1}	[89]
-OH-modified $SrTiO_3$ (OH-STO)	-OH functionalization	Simulated sunlight	701.2 μmol g^{-1} h^{-1} (5.3 times that of $SrTiO_3$)	[91]
Carboxyl-modified PCN (PCN-2AA-3)	-COOH functionalization	Visible light	1692.1 μmol g^{-1} h^{-1}	[99]
S-scheme HOF/WO_3	S-scheme heterojunction	455 nm	475.5 mmol g^{-1} h^{-1} (2.7 times that of HOF)	[137]
CGZS/Ni_9S_8	Schottky heterojunction	Visible light	6.68 mmol g^{-1} h^{-1} (3.6 times that of CGZS)	[143]
ZIS/CoDA/SCN	Tandem heterojunctions	Visible light	15.99 mmol g^{-1} h^{-1}	[153]
H-GDY/O-MoS_{2-x}	Anion vacancy defects	Visible light	2272.97 μmol g^{-1} h^{-1} (25 times that of MoS_2)	[112]

tandem heterojunction [153]. The Co dual atoms modulated the valence band of g-C_3N_4 to achieve band alignment with ZIS and formed an interlayer rapid charge transfer channel through axial coordination with S atoms in ZIS. The H_2 evolution rate of ZIS/CoDA/SCN reached 15.99 mmol g^{-1} h^{-1}, the highest value among g-C_3N_4-supported atomic-level cobalt-based catalysts to date, with interlayer charge delocalization promoting rapid charge transport. Tandem heterojunctions can integrate multiple electron transfer pathways, achieving high activity through multi-mechanism synergy. However, their design is complex, with numerous interfaces and defects, resulting in poor controllability during practical synthesis and making it difficult to avoid interfacial losses. Therefore, while their theoretical performance potential is high, stability and operability remain significant challenges. Future efforts should focus on structural simplification, controllable interfaces, and clear mechanistic understanding.

7. Conclusion and perspectives

This review summarizes recent advances in surface and interface engineering for photocatalytic H_2 evolution, focusing on strategies including elemental doping, functional group modification, defect engineering, and various heterojunction configurations (Table 2). Doping and functionalization can tune band structures and surface active sites. Defect engineering effectively enhances photogenerated carrier separation. Heterojunctions utilize built-in interfacial fields or Z/S-scheme charge transfer mechanisms to achieve spatial separation of electrons and holes. The synergistic effects of these strategies are central to enhancing photocatalytic performance. Surface modifications optimize adsorption/desorption kinetics. Interface engineering facilitates charge transfer. Defects and dopants increase carrier lifetimes and reaction activity. By systematically integrating these strategies, photocatalysts have achieved significant improvements in photogenerated charge separation, reaction kinetics, and light response range. These advancements provide a solid foundation for efficient photocatalytic water splitting. In summary, surface and interface engineering play a critical role in realizing efficient and sustainable photocatalytic H_2 evolution. Ongoing innovation is needed in material stability, low-cost synthesis, and large-scale applications. Synergistic optimization of different strategies and a deeper understanding of interfacial mechanisms will be key to advancing the industrial application of solar-driven H_2 evolution.

Although surface and interface engineering has significantly enhanced the efficiency of photocatalytic H_2 evolution, numerous challenges remain for practical applications. First, the stability of surface and interface structures remains a critical factor limiting the long-term operation of photocatalysts. While elemental doping, functional group modification, and defect engineering can effectively promote the separation and migration of photogenerated carriers. But dopants may migrate or cluster. Functional groups may undergo oxidative degradation. Defects may collapse during prolonged light irradiation or electrochemical conditions, leading to decreased photocatalytic activity. Heterojunction structures are prone to recombination or interfacial phase separation, particularly in nanoscale materials. Interfacial stress and lattice mismatch can lead to a decline in activity and selectivity over time. Therefore, achieving high stability and durability at the surface and interface remains a key research focus (Fig. 8).

(1) Multi-strategy synergistic design. Future optimization of photocatalysts should not be restricted to a single modification route but should instead focus on constructing multidimensional synergistic systems. By systematically integrating element doping, functional-group modification, defect engineering, and heterostructure construction, synergistic improvements can be achieved across band-structure regulation, interfacial charge migration, and surface reaction kinetics. For instance, the development of round-the-clock photocatalytic systems incorporating energy storage mechanisms, such as interfacial charge pools or long-afterglow phosphorescent materials, enables continuous operation under alternating light and dark conditions. These systems sustain H_2 evolution even after illumination ceases, significantly enhancing the stability and practical utility of photocatalytic H_2 evolution throughout natural day-night cycles [154]. The deep incorporation of AI provides new opportunities for the precise design of synergistic modification strategies. Machine-learning models, such as random forests and neural networks, trained on large datasets extracted from the literature can rapidly screen optimal modification combinations.

(2) Precision interface engineering at the atomic/molecular scale. The interfacial structure dictates the actual utilization efficiency of photogenerated charge carriers; therefore, atomic- or molecular-level manipulation is expected to become a dominant trend. Constructing metal single-atom or dual-atom sites, π-π stacked interfaces, directional coordination bonds, or hydrogen-bond networks can precisely regulate local electronic structures and interfacial built-in electric fields, thereby enhancing electron migration rates and the exposure of active sites. On this basis, the introduction of AI and machine learning (ML) will greatly accelerate the discovery and optimization of high-performance materials. AI can predict optimal dopant configurations, interfacial architectures, or stable defect distributions through high-throughput screening. Autonomous experimental platforms combined with robotic synthesis can significantly shorten the cycle from material design to verification. Intelligent models are capable of mining large-scale photocatalytic datasets to uncover key factors governing interfacial charge dynamics, ultimately enabling truly data-driven material design.

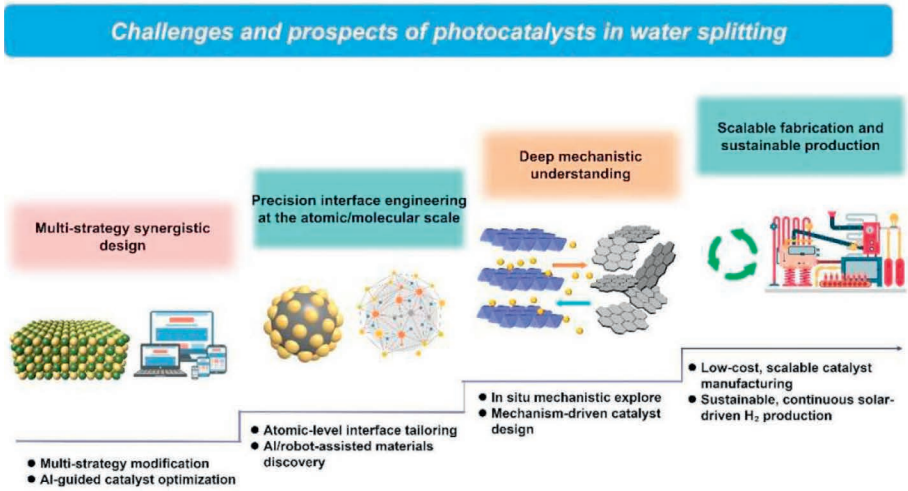


Fig. 8. Challenges and prospects of photocatalysts in water splitting.

(3) Deep mechanistic understanding. A profound understanding of interfacial charge-transfer mechanisms is essential for rational photocatalyst design. Future research should integrate advanced characterization techniques with theoretical simulations to establish a complete mechanistic-analysis framework. *In situ* and *quasi-in situ* techniques, such as *in situ* TEM, *in situ* XPS, *in situ* EPR, and transient absorption spectroscopy, can reveal the dynamic structural evolution under illumination and reaction conditions. DFT calculations, molecular dynamics, and nonadiabatic dynamics simulations can model interfacial electronic behaviors, predict defect states, charge-transfer pathways, and reaction energy barriers. By using experimental data to refine theoretical models, mechanism-driven rather than empirical design becomes possible, significantly accelerating catalyst innovation and providing a solid theoretical foundation for efficient water splitting systems.

(4) Scalable fabrication and sustainable evolution. For the potential deployment of photocatalytic water splitting in sustainable-energy systems, the dissemination of this technology must reconcile catalyst cost, fabrication complexity, and environmental compatibility [24]. First, practical industrial applications require an STH efficiency exceeding 10% and a catalyst lifespan of several years. However, most materials designed through complex surface engineering still face severe challenges regarding structural stability under prolonged, continuous irradiation. Especially for non-oxide narrow-bandgap semiconductors, suppressing photocorrosion through interfacial passivation layers or precise co-catalyst loading is central to determining their service life [155]. Second, cost control is a decisive factor for industrialization. Large-scale deployment requires photocatalytic panel costs to be maintained below 100 USD per square meter. This implies that high-cost surface modification techniques commonly used in laboratories, such as noble metal single-atom loading or complex vacuum deposition processes, must transition toward simpler, mass-producible liquid-phase synthesis or *in-situ* modification strategies. Future research should prioritize optimizing reaction kinetics at the solid-liquid-gas tri-phase interface through micro-nano structural engineering to reduce pumping energy consumption and auxiliary system costs during large-scale operations. Finally, actual outdoor operating environments pose higher requirements for interfacial stability due to temperature fluctuations, intermittent sunlight, and environmental corrosion. Developing robust interfacial systems that can withstand natural day-night cycles, possess self-healing capabilities, or exhibit high tolerance to impurity ions will be key to achieving the economic viability of photocatalytic H_2 evolution. By establishing standardized long-term durability assessment systems and strengthening collaboration between industry and academia, the transition of photocatalytic technology from gram-scale demonstrations to ton-scale production will be effectively accelerated.

The future standardization system for photocatalytic water splitting must prioritize the normalization of experimental methodologies and performance evaluation [155]. Regarding the reaction apparatus, it is essential to define selection criteria for reactor types, including batch and flow systems, while emphasizing enhanced sealing and temperature control to prevent air contamination or back-reaction interference. Gas sampling and detection procedures must be standardized through vacuum-closed circulation or inert-gas-protected flow architectures. In terms of illumination conditions, the framework should unify light-intensity calibration and spectral-matching requirements, alongside the periodic verification of light-source stability. For performance characterization, AQE and STH efficiency must serve as the core metrics, replacing reaction rates solely normalized by catalyst mass. Furthermore, intermediate evacuation experiments are necessary to distinguish catalyst degradation from the effects of the reverse reaction. For practical assessments, the evaluation should incorporate long-term durability, environmental tolerance, and mass-transfer optimization for industrial-grade immobilized catalysts under fluctuating temperature, irradiance, and pH levels. Finally, a professional technical committee should formulate unified reporting formats and data-submission norms. This would ensure that results across different research teams are comparable and reproducible, establishing a solid foundation for the transition from laboratory research to industrial applications.

Overall, the realization of efficient, stable, and scalable photocatalytic water splitting H_2 evolution requires the deep convergence of materials chemistry, interfacial and surface engineering, artificial intelligence, and theoretical computation. Future photocatalyst design will evolve toward system-level synergy, industrial applicability, and data-driven innovation. With the maturation of material platforms, AI-assisted design, and advanced *in situ* characterization, photocatalytic H_2 evolution is expected to play an increasingly critical role in future sustainable-energy systems.

CRediT authorship contribution statement

Xue Zhang: Writing – review & editing, Writing – original draft, Visualization, Investigation, Conceptualization. **Zixuan Zhang:** Visualization, Methodology, Investigation. **Zongyang Ya:** Visualization, Methodology, Investigation. **Shengbo Zhang:** Writing – review & editing, Project administration, Funding acquisition. **Hua Wang:** Project administration, Funding acquisition, Conceptualization.

Declaration of competing interest

The authors declare that they have no known competing financial interests or personal relationships that could have appeared to influence the work reported in this paper.

Acknowledgment

This research was funded by the National Natural Science Foundation of China (Nos. 22178266 and 22572141).

References

[1] A. Slameršak, G. Kallis, D.W. O'Neill, Nat. Commun. 13 (2022) 6932.
[2] T. Zhang, J. Clean. Prod. 216 (2019) 184–196.
[3] S.W. Boettcher, Chem. Rev. 124 (2024) 13095–13098.
[4] V. Tharun, P.S. Kumar, Renew. Sustain. Energy Rev. 224 (2025) 116067.
[5] T. Klatzer, U. Bachhiesl, S. Wogrin, et al., Appl. Energy 355 (2024) 122264.
[6] A. Ganter, K.E. Lonergan, H.M. Büchi, et al., One Earth 7 (2024) 1981–1993.
[7] R.M. Navarro, M.A. Peña, J.L.G. Fierro, Chem. Rev. 107 (2007) 3952–3991.
[8] K. Atsonios, K.D. Panopoulos, A. Doukelis, et al., Energy Convers. Manag. 60 (2012) 196–203.
[9] S. Anwar, X. Li, Front. Energy 17 (2023) 585–610.
[10] B. Wang, Y. Shao, K. Guo, et al., Energy Convers. Manag. 332 (2025) 119777.
[11] L. Guo, Z. Wu, H. Wang, et al., Chem. Eng. J. 455 (2023) 140689.
[12] Y. Xie, C. Xu, Y. Liu, et al., Adv. Sci. 12 (2025) 2410201.
[13] G. Lopez, L. Santamaria, A. Lemonidou, et al., Nat. Rev. Methods Primers 2 (2022) 20.
[14] P. Zhang, Y. Guo, J. Chen, et al., Nat. Catal. 1 (2018) 332–338.
[15] J.G. Arias, Z. Zhang, T.R. Reina, et al., Environ. Chem. Lett. 21 (2023) 3089–3104.
[16] S. Sahil, R. Singh, S.K. Masakapalli, et al., Environ. Chem. Lett. 22 (2024) 1665–1702.
[17] K.G. dos Santos, C.T. Eckert, E. De Rossi, et al., Renew. Sustain. Energy Rev. 68 (2017) 563–571.
[18] S.G. Simoes, J. Catarino, A. Picado, et al., J. Clean. Prod. 315 (2021) 128124.
[19] P. Wang, J. Zheng, X. Xu, et al., Adv. Mater. 36 (2024) 2404806.
[20] M. Liu, Z. Yao, J. Gu, et al., Chem. Eng. J. 461 (2023) 141918.
[21] J. Xie, P. Ma, Z. Fu, Trans. Tianjin Univ. 31 (2025) 590–615.
[22] Z. Zhao, S. Yue, G. Yang, et al., Trans. Tianjin Univ. 30 (2024) 1–26.
[23] P. Zhou, I.A. Navid, Y. Ma, et al., Nature 613 (2023) 66–70.
[24] T. Hisatomi, T. Yamada, H. Nishiyama, et al., Nat. Rev. Mater. 10 (2025) 769–782.
[25] Y. Zhang, D. Ma, J. Li, et al., Coordin. Chem. Rev. 517 (2024) 215995.
[26] H. Su, W. Wang, R. Shi, et al., Carbon Energy 5 (2023) e280.
[27] X. Liu, X. Yang, X. Ding, et al., Chin. Chem. Lett. 34 (2023) 108148.
[28] M.R. Hoffmann, S.T. Martin, W. Choi, et al., Chem. Rev. 95 (1995) 69–96.
[29] X. Li, J. Yu, M. Jaroniec, Chem. Soc. Rev. 45 (2016) 2603–2636.
[30] S. Chen, C. Li, K. Domen, et al., Joule 7 (2023) 2445–2467.
[31] R.D. Tentu, S. Basu, Curr. Opin. Electrochem. 5 (2017) 56–62.
[32] A.A. Ismail, D.W. Bahnemann, Sol. Energy Mater. Sol. Cells 128 (2014) 85–101.
[33] Y. Wang, T. Lee, Y. Lo, et al., Carbon 175 (2021) 223–232.
[34] Y. Liu, F. Zheng, H. Dai, et al., Angew. Chem. Int. Ed. 62 (2023) e202302126.
[35] T. He, Y. Zhao, D. Benetti, et al., J. Am. Chem. Soc. 146 (2024) 27080–27089.
[36] H. Nishiyama, T. Yamada, M. Nakabayashi, et al., Nature 598 (2021) 304–307.
[37] S. Bai, W. Jiang, Z. Li, et al., ChemNanoMat 1 (2015) 223–239.
[38] D. Bhalothia, A. Beniwal, H. Gurjar, et al., Small 21 (2025) e06018.
[39] H. Xu, H. Shang, C. Wang, et al., Coordin. Chem. Rev. 418 (2020) 213374.
[40] B. Zhou, R. Gao, J. Zou, et al., Small 18 (2022) 2202336.
[41] S. Sun, B. Peng, Y. Song, et al., Chem. Eng. J. 495 (2024) 153547.
[42] F. Yu, L. Wang, Q. Xing, et al., Chin. Chem. Lett. 31 (2020) 1648–1653.
[43] X. Pei, J. Bian, W. Zhang, et al., Adv. Funct. Mater. 34 (2024) 2400542.
[44] Y. Akinaga, T. Kawawaki, H. Kameko, et al., Adv. Funct. Mater. 33 (2023) 2303321.
[45] P. Guo, X. Liu, C. You, et al., Appl. Catal. B: Environ. Energy 366 (2025) 125011.
[46] R. Li, J. Luan, Y. Zhang, et al., Renew. Sustain. Energy Rev. 206 (2024) 114863.
[47] M.A. Zaed, K.H. Tan, R. Saidur, et al., Trans. Tianjin Univ. 31 (2025) 524–553.
[48] Y. Guo, X. Tan, T. Yu, et al., Adv. Funct. Mater. 36 (2026) e22276.
[49] J. Teng, W. Li, Z. Wei, et al., Angew. Chem. Int. Ed. 63 (2024) e202416039.
[50] J. Su, J. Zhang, S. Chai, et al., Nano Mater. Sci. 8 (2026) 351–363.
[51] F. Qiao, Nano Res. Energy 4 (2025) e9120132.
[52] X. Guo, X. Wan, Q. Liu, et al., eScience 2 (2022) 304–310.
[53] J.F. Guayaquil Sosa, B. Serrano Rosales, P.J. Valadés Pelayo, et al., Appl. Catal. B: Environ. 211 (2017) 337–348.
[54] G. Iervolino, O. Tammaro, M. Fontana, et al., J. Energy Chem. 101 (2025) 263–277.
[55] D. Xiang, J. Yang, H. Xie, et al., Chem. Eng. J. 525 (2025) 169994.
[56] L. Bao, S. Ali, C. Dai, et al., ACS Nano 18 (2024) 5878–5889.
[57] H. Hu, K. Zhang, G. Yan, et al., Chin. J. Catal. 43 (2022) 2332–2341.
[58] H.J. Song, L.Y. Luo, S.Y. Wang, et al., Chin. Chem. Lett. 35 (2024) 109347.
[59] C. Cai, H. Lu, C. Cheng, et al., Trans. Tianjin Univ. 31 (2025) 555–566.
[60] V. Bharathi Mohan, S. Jayachitra, P. Devi, et al., Chem. Eng. J. 515 (2025) 163331.
[61] D. Yang, Q. Ye, C. Qu, et al., Appl. Catal. B: Environ. Energy 361 (2025) 124637.
[62] B. Chen, A. Mansouri, C.M. RuedaNavarro, et al., Adv. Energy Mater. 15 (2025) 2500211.
[63] C. Yang, J. Le, Y. Kuang, et al., J. Am. Chem. Soc. 146 (2024) 26198–26206.
[64] D. Ontiveros, S. Vela, F. Viñes, et al., Energy Environ. Mater. 7 (2024) e12774.
[65] A.T. Isa, H.Y. Hafeez, J. Mohammed, et al., J. Alloys Compd. 1005 (2024) 175951.
[66] H.Y. Chung, R.J. Wong, H. Wu, et al., Adv. Energy Mater. 15 (2025) 2404956.
[67] Z. Yuan, B. Yan, M. Li, et al., Int. J. Hydrogen Energy 145 (2025) 412–432.
[68] A. Kudo, Y. Miseki, Chem. Soc. Rev. 38 (2009) 253–278.
[69] D. Wang, T. Sheng, J. Chen, et al., Nat. Catal. 1 (2018) 291–299.
[70] Q. Zhang, J. Chen, H. Che, et al., ACS Mater. Lett. 4 (2022) 2166–2186.
[71] M.J. Molaei, Fuel 365 (2024) 131159.
[72] T. Guo, H. Fei, R. Liu, et al., Adv. Funct. Mater. 34 (2024) 2407406.
[73] J.K. Nørskov, J. Rossmeisl, A. Logadottir, et al., J. Phys. Chem. B 108 (2004) 17886–17892.
[74] J. Wang, M. Zhang, Z. Chen, et al., ACS Energy Lett. 9 (2024) 653–661.
[75] Z. He, Y. Xia, G. He, et al., Chem. Eng. J. 506 (2025) 159957.
[76] G. Yang, M. Dou, D. Li, et al., Chem. Eng. J. 521 (2025) 166752.
[77] B. He, Y. Cao, K. Lin, et al., eScience 5 (2025) 100242.
[78] L. Bao, Y. Jia, X. Ren, et al., J. Mater. Sci. Technol. 199 (2024) 75–85.
[79] F. Qin, Y. Kang, X. San, et al., J. Am. Chem. Soc. 147 (2025) 12897–12907.
[80] B. Xiao, C. Shen, Z. Luo, et al., Chem. Eng. J. 499 (2024) 156331.
[81] Y. Li, H. Zhou, S. Cai, et al., Nat. Catal. 7 (2024) 77–88.
[82] T. Wang, X. Pan, M. He, et al., Adv. Sci. 11 (2024) 2403771.
[83] B. Li, H. Zheng, T. Zhou, et al., Chem. Eng. J. 497 (2024) 154726.
[84] S. Guemou, F.E. Haq, C. Cheng, et al., Chem. Eng. J. 526 (2025) 170746.
[85] G. Wu, Z. He, Q. Wang, et al., J. Mater. Sci. Technol. 195 (2024) 1–8.
[86] Q. Tian, L. Wang, W. Sun, et al., Appl. Catal. B: Environ. Energy 359 (2024) 124516.
[87] M. Duan, S. Guo, W. Niu, et al., J. Am. Chem. Soc. 147 (2025) 38599–38608.
[88] S. Liu, J. Zhan, C. Yang, et al., Appl. Catal. B: Environ. Energy 380 (2026) 125803.
[89] Z. Su, C. Ye, Y. Xu, et al., Chem. Eng. J. 496 (2024) 154282.
[90] H. Wang, L. Yu, J. Peng, et al., J. Mater. Sci. Technol. 208 (2025) 111–119.
[91] Y. Jiang, J. Xie, Z. Lu, et al., J. Colloid Interface Sci. 612 (2022) 111–120.
[92] J. Hu, L. Wu, H. Liu, et al., J. Mater. Chem. A 12 (2024) 4854–4865.
[93] C. Du, J. Feng, S. Xu, et al., Int. J. Hydrogen Energy 53 (2024) 280–289.
[94] N. Wang, L. Cheng, X. Zhang, et al., Int. J. Hydrogen Energy 69 (2024) 1394–1402.
[95] M. Ma, R. Lin, K. Huang, et al., Carbon Energy 7 (2025) e70029.
[96] X. Zhang, L. Jian, L. Wang, et al., Appl. Surf. Sci. 571 (2022) 151304.
[97] L. Mao, B. Lu, J. Shi, et al., Catal. Today 409 (2023) 94–102.
[98] X. Zhong, Y. Zhu, Y. Wang, et al., Small 20 (2024) 2402219.
[99] Y. Liang, C. Cao, L. Zeng, et al., J. Mater. Chem. A 12 (2024) 26096–26102.
[100] G. Gao, L. Zhang, Q. Chen, et al., Chem. Eng. J. 409 (2021) 127370.
[101] N. Wang, Y. Zhang, Z. Meng, et al., Int. J. Hydrog. Energy 171 (2025) 151243.
[102] T. Huang, K. Lin, Y. Zhuang, et al., Sci. Adv. 11 (2025) eadx1629.
[103] S. Tang, Y. Xu, X. Hu, et al., J. Colloid Interface Sci. 648 (2023) 898–906.
[104] W. Zhou, H. Huang, Z. Wang, et al., J. Mater. Chem. A 12 (2024) 4046–4056.
[105] X. Wan, C. Yang, W. Shi, et al., Small 22 (2026) 2504146.
[106] X. Leng, K. Yang, L. Sun, et al., Angew. Chem. Int. Ed. 64 (2025) e202416992.
[107] J. Kim, J. Jeon, Y.H. Kim, et al., Angew. Chem. Int. Ed. 63 (2024) e202319395.
[108] K. Li, T. Xiao, J. Tang, et al., Appl. Catal. B: Environ. Energy 371 (2025) 125201.
[109] L. Hao, R. Shen, G. Liang, et al., Appl. Catal. B: Environ. Energy 348 (2024) 123837.
[110] F. Yu, L. Wang, Q. Xing, et al., Chin. Chem. Lett. 31 (2020) 1648–1653.
[111] Y. Gu, Y. Han, Y. Li, et al., Chem. Eng. J. 502 (2024) 158084.
[112] L. Fan, Z. An, Q. Xiao, et al., Appl. Catal. B: Environ. Energy 363 (2025) 124821.
[113] Z. Chen, L. Wang, X. Jiao, et al., Chem. Eng. J. 517 (2025) 164289.
[114] Q. Pang, Y. Wu, Y. Yang, et al., Chem. Eng. J. 525 (2025) 170098.
[115] U. Sahoo, S. Pattnayak, S. Choudhury, et al., Appl. Catal. B: Environ. 343 (2024) 123524.
[116] X. Guo, L. Fan, J. Liu, et al., Appl. Catal. B: Environ. Energy 378 (2025) 125586.
[117] E. Zhao, J. Su, H. Fan, et al., Green Energy Environ. 11 (2026) 557–564.
[118] D. Liu, C. Zhang, J. Shi, et al., Small 20 (2024) 2310289.
[119] C. Zheng, Y. Guo, C. Zhang, et al., Appl. Catal. B: Environ. Energy 365 (2025) 124879.
[120] J. Xiao, Y. Chen, C. Cai, et al., Small 21 (2025) 2503335.
[121] J. Zhang, L. Li, M. Du, et al., Small 19 (2023) 2300402.
[122] L. Tian, Y. Wu, H. Kang, et al., Adv. Funct. Mater. 35 (2025) 2509584.
[123] Y. Sun, X. Pei, B. Wang, et al., Chem. Eng. J. 463 (2023) 142488.
[124] Y. Guo, T. Xue, J. Kuang, et al., Adv. Funct. Mater. 36 (2026) e22083.

[125] X. Wang, T. Shi, X. Wang, et al., Appl. Catal. B: Environ. Energy 348 (2024) 123807.
[126] Y. Quan, J. Li, X. Li, et al., Appl. Catal. B: Environ. Energy 362 (2025) 124711.
[127] Y. Quan, R. Li, X. Li, et al., Small 20 (2024) 2406576.
[128] D. Zhang, C. Zhang, G. Zhao, et al., Chem. Eng. J. 505 (2025) 159567.
[129] G. Jia, Y. Wang, X. Cui, et al., Matter 5 (2022) 206–218.
[130] Y. Zheng, Y. Wang, S. Mansoor, et al., Small 20 (2024) 2311725.
[131] X. Chen, Q. Zhang, Y. Wang, et al., J. Mater. Sci. Technol. 238 (2025) 86–96.
[132] X. Wang, T. Shi, X. Wang, et al., J. Energy Chem. 92 (2024) 151–161.
[133] Z. Lian, F. Wu, J. Zi, et al., J. Am. Chem. Soc. 145 (2023) 15482–15487.
[134] T. Xu, Y. Xie, S. Qi, et al., Angew. Chem. Int. Ed. 63 (2024) e202409945.
[135] Y. Yuan, J.N. Pan, W.N. Yin, et al., Chin. Chem. Lett. 35 (2024) 108724.
[136] J. Cheng, B. Cheng, J. Xu, et al., eScience 5 (2025) 100354.
[137] H. Niu, G. Zhu, S. Zhang, et al., Chem. Eng. J. 525 (2025) 170181.
[138] T. Gao, X. Liu, K. Wang, et al., J. Colloid Interface Sci. 692 (2025) 137475.
[139] K. Gao, Q. He, L. Zhang, et al., ACS Catal. 15 (2025) 5155–5170.
[140] Y. Zhou, K. Gao, Y. Song, et al., Appl. Catal. B: Environ. Energy 382 (2026) 126002.
[141] H. Hu, X. Sun, Y. Ma, et al., Adv. Mater. 37 (2025) e10193.
[142] X. Li, J. Li, Y. Mao, et al., Adv. Funct. Mater. 36 (2026) e21171.
[143] Y. Li, S. Wang, J. Chen, et al., Adv. Energy Mater. 16 (2026) e04755.
[144] J. Deng, J. Liang, Z. Hu, et al., Appl. Catal. B: Environ. Energy 378 (2025) 125593.
[145] T. Guo, C. Wang, L. Chen, et al., Compos. Part B: Eng. 305 (2025) 112766.
[146] Z. Zhou, Z. Jin, Chin. J. Catal. 74 (2025) 294–307.
[147] W.X. Zhang, J.T. Hou, M. Bai, C. He, J.R. Wen, Chin. Chem. Lett. 34 (2023) 108270.
[148] F. Mi, Z. Fang, J. Li, et al., Adv. Funct. Mater. 35 (2025) 2506838.
[149] X. Chu, S. Liu, B. Luan, et al., Angew. Chem. Int. Ed. 64 (2025) e202422940.
[150] Y. Wang, P. Maity, Z. Liu, et al., Adv. Mater. 37 (2025) 2415161.
[151] J. Yang, B. Ma, Y. Zhu, Appl. Catal. B: Environ. Energy 381 (2026) 125890.
[152] X. Yang, Q. Xiao, S. Zhang, et al., Sep. Purif. Technol. 382 (2026) 136096.
[153] Y. Wei, L. Jin, D. Kong, et al., Chem. Eng. J. 516 (2025) 164123.
[154] B. Kaur, P. Singh, D.A. Dinh, et al., Trans. Tianjin Univ. 31 (2025) 645–668.
[155] T. Takata, L. Lin, T. Hisatomi, et al., Adv. Mater. 36 (2024) 2406848.